Prediction and delay of 2D laminar boundary layer separation near leading edges

Anna Dostovalova

Acknowledgements

This work contains no material which has been accepted for the award of any other degree or diploma in any university or other tertiary institution and, to the best of my knowledge and belief, contains no material previously published or written by another person, except where due reference has been made in the text.

I consent to this copy of my thesis, when deposited in the University Library, being available for loan and photocopying.

Abstract

Boundary-layer flows near leading edges of generally curved obstacles have been studied for a long time. Apart from having many practical applications, the theory and approaches prevailing in this area stimulate development of a variety of computational tools and form a ground for testing them.

The specific aim of this work is to study two-dimensional laminar boundary layer flows near the leading edges of airfoils and other elongated bodies, and to explore geometries for which boundary layer separation can be avoided. This class of problems is relevant to optimal design of wings, aircraft and projectile noses, laminar flow control methods and adaptive wing technology. One of the findings of this work suggests that local modifications to parabolic wing noses can yield up to 11% increase in the unseparated angle of attack. Another result obtained here is the set of shortest possible generalised elliptic noses of long symmetric bodies which allow unseparated flow.

Methods adopted in this work are based on the combined use of numerically solved Prandtl equations written in Görtler variables, and inviscid solutions obtained semi-analytically by the conformal mapping method. The resulting technique being reliable, fast and computationally inexpensive, can complement or test the results obtained using a comprehensive CFD approach.

Contents

Introduction

Boundary-layer flows near leading edges of generally curved obstacles have been studied for some time [36, 25, 33, 30]. Apart from having many practical applications, the theory and approaches prevailing in this area stimulate development of a variety of computational tools and form a ground for testing them.

Computational Fluid Dynamics is now perceived by many as a separate branch of applied mathematics. The idea to reduce solution of complex fluid mechanics problems to operating solvers has created a new field of specialisation. The resulting technology successfully employs the effort of programmers and engineers at different stages of computation: from grid and input data generation, and model description, to postprocessing and visualisation. Flows thus computed and their parameters are subsequently used in the design of actual aircrafts and vessels.

The comprehensive CFD approach, in which the full viscous flow is computed for an exact, or very similar, aircraft/vessel geometry does not eliminate the need for approximate semi-analytic techniques, which, though allowing us to consider only simplified geometries, can yield an alternative solution and yet be less computationally demanding (e.g. see the review [2]

where the set-up and grid generation costs for CFD routines are discussed).

Local behaviour of the stream near some elements of aircrafts and vessels can often be approximated with a boundary layer flow past a leading edge. Prandtl's equations [24, 26, 23] have been used for description of laminar boundary layers since 1905 [12]. In particular, they provided an explanation for the phenomenon known as *separation* of flow from the surface of the obstacle.

Being a cause of flow instability and strong drag, separation of boundary layers is usually considered as something which should be avoided [9]. One of the techniques used for avoiding boundary layer separation called *laminar flow control* [13] is based on a *steady suction* (slot, porous and perforated suction), *thermal control* and *wave management* [29].

Resulting savings in fuel consumption due to drag reduction (up to 14 % for some models [13]) can outweigh increased design costs associated with the laminar flow control. In addition, the suction and thermal control requirements can be reduced by using wing geometry considerations. The corresponding technique is referred to as the *hybrid laminar flow control*. Naturally, such a technique requires understanding of laminar boundary flow behaviour and its dependence on the wing geometry. Our primary goal here is to study laminar boundary layer flows near the leading edges of airfoils and similar bodies and to explore geometries for which boundary layer separation can be avoided. This class of problems is also of a direct relevance to the adaptive wing technology [29].

The work is organised in three chapters, and each of them considers a specific body geometry.

In Chapter 1 we study local laminar boundary layer flows past near-

parabolic noses of thin airfoils, modelling such noses by semi-infinite bodies. We suggest nose modifications which delay separation of the boundary layer to greater values of the angle of attack, thus permitting greater lift before stall is reached. Here we also provide details of the numerical procedure we use for computation of the laminar boundary layer. Our approach is based on the technique developed by Werle and Davis [36]. This is one of a family of methods for obtaining exact solutions of the full Prandtl boundary layer equations using finite differences (see [37] and other papers referenced in [37]). Alternative methods for the approximate calculation of boundary layers which use momentum integral relations and *a priori* velocity profiles [37, 11, 7, 8] may reduce computational cost, but are also likely to give different results for separation characteristics due to strong sensitivity of the solution to the shape of the boundary.

In Chapter 2 we consider finite-length general airfoils. We revisit here the Theodorsen–Naiman method for computation of the potential flow about a complete airfoil, incorporating it into a convenient graphical user interface, which allows one to perform visual manipulations needed for improvement of convergence of the iterative procedure. We also discuss the limits of the method's applicability to computation of laminar boundary layers for very long thin airfoils. The resulting program thus allows solution for flows about arbitrary user-defined airfoils. In that sense, it has similar objectives to packages such as XFOIL by M. Drela [8], MELFOIL by M. S. Garelik, PROFIL by R. Eppler and other packages, noting that XFOIL [7, 8] also couples the potential flow with an approximate boundary layer solution.

In Chapter 3 we show how the technique considered in Chapter 2 can be modified to make it applicable to the study of boundary layers in flows past

long objects. We then consider a particular family of smoothly curving front faces or noses of length L and width H attached to a semi-infinite plate of finite width, and use the developed procedure to determine the front face profile, allowing an unseparated flow, for which the aspect ratio L/H of the nose is minimal.

Results of Chapters 1 and 2 have been previously published by the author in papers and reports [6, 34, 28, 27].

Chapter 1

Airfoil nose shapes delaying leading-edge separation when at angles of attack

1.1 Introduction

Smoothly-shaped leading edges, including features such as drooped noses, have a long history of favourable use for improving lift generation in aerodynamics, see e.g. [3]. In the present chapter, our aim is choose a nose shape that postpones separation of the boundary layer on the upper surface of a lifting airfoil to the highest possible angle of attack.

The simplest type of smooth leading edge is one that appears locally to be exactly parabolic, with a radius of curvature r which is small compared to the airfoil's chord c. The upper $(+)$ and lower $(-)$ surfaces of such an airfoil could then be written near to the nose $x = 0$ as

$$y \simeq \pm\sqrt{2rx}. \tag{1.1}$$

10

For such noses, Ruban [25] and Tuck [33] have shown that the upper-surface laminar boundary layer has everywhere-positive wall shear stress if the angle of attack α (relative to the "ideal" value [1] if the airfoil is cambered) satisfies $\alpha < \alpha_0$, where $\alpha_0 = 0.818\sqrt{r/c}$. When $\alpha \approx \alpha_0$, the shear stress becomes small and ultimately vanishes in a broad region well downstream of the actual nose, though still within the leading-edge region at about $x \approx 9r$.

The class of thin airfoils of interest in the present chapter is one possessing a well-defined "apparent" leading-edge radius of curvature r, but nevertheless having a non-simply curved leading-edge shape. That is, the airfoil nose still appears parabolic and given by (1.1) when seen in an "intermediate" region $r \ll x \ll c$ which is many nose radii away from the leading edge but much closer to the leading edge than the trailing edge. However, when examined more finely near the leading edge with $x = O(r)$, the nose reveals a non-parabolic shape with equation

$$y = \pm\sqrt{2rx}\, g_\pm(x/r) \tag{1.2}$$

where $g_\pm(X)$ are smooth positive functions for $X > 0$ satisfying $g_\pm(X) \to 1$ as $X \to \infty$.

We choose a family of nose-shape functions $g_\pm(X)$, and compute upper surface boundary layers for a range of angles of attack α up to the separation value α_0, selecting members of that family which maximise α_0. The resulting "optimum" nose shapes tend to be slightly sharper than parabolas, and if allowed to be unsymmetrical, are also slightly drooped.

An important feature of the boundary layer on these shaped noses is that for $\alpha \approx \alpha_0$, there is a highly-localised separation crisis quite close to the most forward point of the nose, where the shear stress almost vanishes. If this crisis is avoided, the boundary layer remains unseparated until there is a

Anna Dostovalova, The University of Adelaide

second broader crisis, located much further downstream, at a similar position to that for the parabolic nose. The optimum noses are then those in which these two crises are forced to occur at the same angle of attack.

There are applications (such as to control surfaces or masts of sailing boats) where symmetry is required by the design, and our results show the possibility of at least a 9% increase in the unseparated angle of attack for such symmetrical airfoils, i.e. to $\alpha_0 = 0.897\sqrt{r/c}$, by sharpening the extreme nose region.

If asymmetry is permitted, in principle an arbitrary amount of improvement is possible by use of a large droop in the nose, but beyond a certain point, this effectively reduces the over-all angle of attack of the airfoil and hence the lift achieved. The whole problem must then be re-examined on a chord-wise scale rather than just locally to the airfoil's nose on the scale of the nose radius of curvature. Meanwhile, however, we can show cases where the droop is acceptably small, but nevertheless where we can achieve better than an 11% increase in the unseparated angle of attack relative to that for a parabolic nose, e.g. to $\alpha_0 = 0.912\sqrt{r/c}$.

1.2 Boundary Layer Equations

1.2.1 Prandtl's Equations

Steady two-dimensional laminar flow of a viscous fluid near a curved surface is governed by Prandtl's boundary layer equations (e.g. [24, 26]):

$$\frac{\partial \bar{u}}{\partial \bar{s}} + \frac{\partial \bar{v}}{\partial \bar{n}} = 0 \; , \tag{1.3}$$

$$\bar{u}\frac{\partial \bar{u}}{\partial \bar{s}} + \bar{v}\frac{\partial \bar{u}}{\partial \bar{n}} = U_e(\bar{s})\frac{dU_e}{d\bar{s}} + \nu\frac{\partial^2 \bar{u}}{\partial \bar{n}^2} \; , \tag{1.4}$$

Anna Dostovalova, The University of Adelaide

where

- $\bar{s}$ and $\bar{n}$ are coordinates measured along and normal to the surface,

- $\bar{u}$ and $\bar{v}$ are the respective velocities,

- $U_e(\bar{s})$ is the inviscid flow velocity at the boundary and ν is the kinematic viscosity.

Let U_∞ denote the speed of the uniform flow far upstream and L be a characteristic length. Equations (1.3)–(1.4) are usually written in the non-dimensional variables
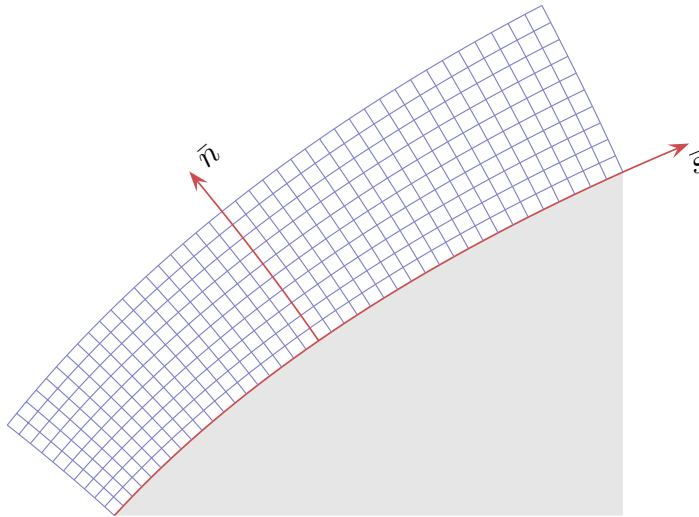

Figure 1.1: The $(\bar{s}, \bar{n})$-coordinate system

$$s = \bar{s}/L, \quad n = \sqrt{\text{Re}}\,\bar{n}/L \ ,$$

$$u = \bar{u}/U_\infty, \quad v = \sqrt{\text{Re}}\,\bar{v}/U_\infty \ ,$$

where Re is the Reynolds number defined as

$$\text{Re} = U_\infty L/\nu \ . \tag{1.5}$$

The non-dimensional form of (1.3)–(1.4) is

$$\frac{\partial u}{\partial s} + \frac{\partial v}{\partial n} = 0 \ , \tag{1.6}$$

$$u\frac{\partial u}{\partial s} + v\frac{\partial u}{\partial n} = u_e(s)\frac{du_e}{ds} + \frac{\partial^2 u}{\partial n^2} \ , \tag{1.7}$$

where $u_e(s) = U_e(sL)/U_\infty$.

The boundary conditions for (1.6)–(1.7) are

$$u(s,0) = v(s,0) = 0, \tag{1.8}$$

$$u(s) \to u_e(s) \quad \text{as } n \to \infty. \tag{1.9}$$

With the introduction of the Görtler variables (ξ, η) and (F, V) defined as

$$\xi = \int_0^s u_e(s)ds, \quad \eta = \frac{u_e}{\sqrt{2\xi}}\,n \ , \tag{1.10}$$

$$u = Fu_e, \quad v = \frac{u_e}{2\xi}V - \frac{\partial \eta}{\partial s}\sqrt{2\xi}F \ , \tag{1.11}$$

this system is transformed into

$$2\xi F_\xi + F + V_\eta = 0 \ , \tag{1.12}$$

$$2\xi F F_\xi + V F_\eta + \sigma^p(\xi)(F^2 - 1) = F_{\eta\eta} \ , \tag{1.13}$$

where

$$\sigma^p(\xi) = \frac{2\xi u'_e(s(\xi))}{u_e^2(s(\xi))} \ . \tag{1.14}$$

The derivations are provided in Section 1.2.2.

The boundary conditions for $F(\xi, \eta)$ and $V(\xi, \eta)$ are

$$F(\xi, 0) = V(\xi, 0) = 0 \quad \text{and} \quad \lim_{\eta \to \infty} F(\xi, \eta) = 1 \ . \tag{1.15}$$

Prandtl's equations in this form are convenient for numerical study of laminar boundary layer flows in the presence of a leading edge, in this case the computation can be started from the stagnation point.

Werle and Davis [36] used equations (1.12)–(1.13) for computation of boundary layer flows past parabolic noses.

1.2.2 Prandtl's equations in Görtler's variables

Here we verify the fact that the transformation of variables (1.10)–(1.11) reduces (1.6)–(1.7) to (1.12)–(1.13).

If $u_e(s)$ is given, s and n are independent variables and

$$\xi(s, n) = \int_0^s u_e(s)ds \quad \text{and} \quad \eta(s, n) = \frac{u_e(s)}{\sqrt{2\xi}} \, n,$$

then

$$\xi_s = u_e(s), \quad \xi_n = 0, \quad \eta_s = \frac{\partial}{\partial s}\left[\frac{u_e(s)}{\sqrt{2\xi}}\right] n, \quad \eta_n = \frac{u_e(s)}{\sqrt{2\xi}} \ . \tag{1.16}$$

Furthermore,

$$u_s = u_\xi \xi_s + u_\eta \eta_s = u_\xi u_e + u_\eta \eta_s \ ,$$

$$u_n = u_\xi \xi_n + u_\eta \eta_n = u_\eta u_e / \sqrt{2\xi} \ ,$$

$$v_n = v_\xi \xi_n + v_\eta \eta_n = v_\eta u_e / \sqrt{2\xi} \ .$$

First obtain the continuity equation in terms of "old" unknowns and "new" variables:

$$u_\xi u_e + u_\eta \eta_s + v_\eta u_e / \sqrt{2\xi} = 0 . \tag{1.17}$$

Also write

$$(u_e)_\xi = u'_e(s)s'(\xi) = u'_e/u_e$$

(henceforth, $u'_e \equiv u'_e(s)$). Now rewrite (1.17) in terms of F and V defined by

$$u = F u_e, \quad v = \frac{u_e}{\sqrt{2\xi}} V - \eta_s \sqrt{2\xi} F .$$

We obtain after substitution into (1.17)

$$(F u_e)_\xi u_e + (F u_e)_\eta \eta_s + \left[\frac{u_e}{\sqrt{2\xi}} V - \eta_s \sqrt{2\xi} F \right]_\eta \frac{u_e}{2\xi} = 0.$$

Hence

$$F_\xi u_e^2 + F u'_e + F_\eta u_e \eta_s + \left[\frac{u_e}{\sqrt{2\xi}} V_\eta - \frac{\partial \eta_s}{\partial \eta} \sqrt{2\xi} F - \eta_s \sqrt{2\xi} F_\eta \right] \frac{u_e}{\sqrt{2\xi}} = 0$$

and

$$F_\xi u_e^2 + F u'_e + \left[\frac{u_e}{\sqrt{2\xi}} V_\eta - \frac{\partial \eta_s}{\partial \eta} \sqrt{2\xi} F \right] \frac{u_e}{\sqrt{2\xi}} = 0 . \tag{1.18}$$

Since $\eta = \eta(s(\xi), n(\xi, \eta))$ we have

$$\begin{cases} \eta_s s'(\xi) + \eta_n n_\xi = 0 \\ \eta_s \cdot 0 + \eta_n n_\eta = 1 \quad (\Rightarrow \ \eta_n = 1/n_\eta) , \end{cases}$$

we obtain

$$\eta_s = -\frac{\eta_n n_\xi}{s'(\xi)} = -\frac{n_\xi}{n_\eta s'(\xi)} = -u_e \frac{n_\xi}{n_\eta} = -\frac{u_e^2}{\sqrt{2\xi}} \left[\frac{\sqrt{2\xi}}{u_e} \right]_{\xi} \eta$$

$$= -\frac{u_e^2}{\sqrt{2\xi}} \left(\frac{1}{\sqrt{2\xi} u_e} - \frac{\sqrt{2\xi}}{u_e^2} u'_e s'(\xi) \right) \eta = \left(-\frac{1}{2\xi} u_e + \frac{u'_e}{u_e} \right) \eta$$

and

$$(\eta_s)_\eta = -\frac{u_e}{2\xi} + \frac{u_e'}{u_e} \ .$$

Hence the equation (1.18) can be reduced to

$$F_\xi u_e^2 + F u_e' + \left(\frac{u_e^2}{2\xi}V_\eta - F\left[u_e' - u_e^2/(2\xi)\right]\right) = 0$$

$$\Rightarrow\ 2\xi F_\xi + F + V_\eta = 0,$$

as required.

Now turn to the momentum equation:

$$u\frac{\partial u}{\partial s} + v\frac{\partial u}{\partial n} = u_e u_e' + \frac{\partial^2 u}{\partial n^2}$$

$$\Downarrow$$

$$u(u_\xi u_e + u_\eta \eta_s) + v u_\eta \frac{u_e}{\sqrt{2\xi}} = u_e u_e' + u_{\eta\eta}\frac{u_e^2}{2\xi} \ .$$

Rewrite this in terms of F and V

$$F u_e \left(F_\xi u_e^2 + F u_e' + F_\eta u_e \eta_s\right)$$
$$+ \left(\frac{u_e V}{\sqrt{2\xi}} - \eta_s \sqrt{2\xi}F\right)F_\eta \frac{u_e^2}{\sqrt{2\xi}} = u_e u_e' + (u_e F)_{\eta\eta}\frac{u_e^2}{2\xi} \ .$$

Simplify to obtain

$$F_\xi F u_e^3 + F^2 u_e' u_e + \frac{F_\eta u_e^3 V}{2\xi} = u_e u_e' + \frac{u_e^3}{2\xi}F_{\eta\eta} \ .$$

Hence

$$2\xi F F_\xi + V F_\eta + \frac{2\xi u_e'}{u_e^2}[F^2 - 1] = F_{\eta\eta},$$

as required.

1.3 Numerical Approach

The system (1.12)–(1.13) subject to (1.15) will be solved for various families of surface shapes and results will be discussed in terms of the skin friction factor

$$\tau = \left.\frac{\partial F}{\partial \eta}\right|_{\eta=0}.$$

The flow is unseparated if $\tau > 0$ for all ξ. For some flows (in particular for those of present interest at low angles of attack) τ remains positive for all ξ, and the flow can be continued with increasing ξ indefinitely. In other cases, (in particular, at high angles of attack) τ goes negative at some $\xi > 0$ and separation of the flow occurs. When separation is imminent, there is a minimum in τ as a function of ξ, whose value reduces as the control parameter β (i.e. angle of attack) is increased, until this minimum value becomes zero, then goes negative. We cease computations when τ becomes zero.
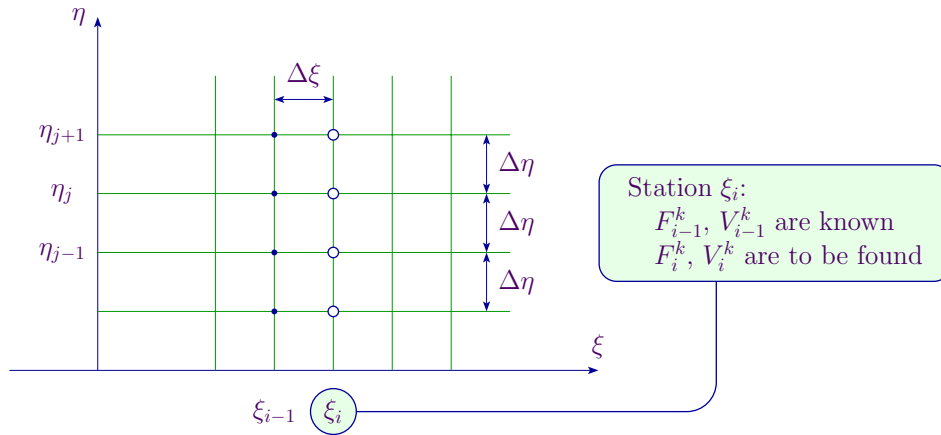

Figure 1.2: Mesh for the numerical procedure

Our numerical procedure is quite straightforward, and the mesh is shown in Figure 1.2. Using central differences for approximating derivatives in (1.12)–(1.13), we rewrite (1.13) in the form of a tridiagonal system with values of the function F across the boundary layer as unknowns, with coefficients dependent on the values of F, V and $\sigma^p(\xi)$ at the previous station in ξ, and on values of F and V which are yet to be determined.

More specifically, the finite difference equations at the beginning of the iteration loop for station ξ_i are

$$2\xi_i F_{i-1}^j \left(\frac{F_i^j - F_{i-1}^j}{\Delta\xi} \right) + V_{i-1}^j \frac{F_i^{j+1} - F_i^{j-1}}{2\Delta\eta}$$

$$+ \sigma_i^p \left((F_{i-1}^j)^2 - 1 \right) = \frac{F_i^{j-1} - 2F_i^j + F_i^{j+1}}{(\Delta\eta)^2} , \qquad (1.19)$$

$$F_i^0 = 0; \quad F_i^J = 1 ,$$

where $j = 1, \ldots, J$, and F_i^j and V_i^j denote $F(\xi_i, \eta_j)$ and $V(\xi_i, \eta_j)$ respectively. Equations (1.19) can be written as a tridiagonal system:

$$A_j F_i^{j-1} + B_j F_i^j + C_j F_i^{j+1} = D_j, \qquad (j = 1, \ldots, J), \qquad (1.20)$$

where

$$
\begin{aligned}
A_j &= -\frac{V_{i-1}^j}{2\Delta\eta} - \frac{1}{(\Delta\eta)^2} , \\
B_j &= \frac{2\xi_i F_{i-1}^j}{\Delta\xi} + \frac{2}{(\Delta\eta)^2} , \\
C_j &= \frac{V_{i-1}^j}{2\Delta\eta} - \frac{1}{(\Delta\eta)^2} , \\
D_j &= \left(F_{i-1}^j \right)^2 \left(\frac{2\xi_i}{\Delta\xi} - \sigma_i^p \right) + \sigma_i^p .
\end{aligned}
\qquad (1.21)
$$

The matrix of the linear system (1.21) has the form

$$
\begin{pmatrix}
B_1 & C_1 & 0 & \cdots & & \cdots & 0 \\
A_2 & B_2 & C_2 & \ddots & & \cdots & \vdots \\
0 & A_3 & \ddots & \ddots & & \ddots & \vdots \\
\vdots & \ddots & \ddots & \ddots & & \ddots & 0 \\
0 & \cdots & 0 & A_{J-1} & & B_{J-1} & C_{J-1} \\
0 & \cdots & \cdots & 0 & & A_J & B_J
\end{pmatrix}
$$

Equations (1.20) are solved using Gaussian elimination. Once F_i^j have been obtained we solve (1.12) discretized as

$$
V_i^j = V_i^{j-1} - \Delta\eta \left(\frac{2\xi_i}{\Delta\xi}(F_i^j - F_{i-1}^j) + F_i^j \right)
$$

$$
V_i^0 = 0 .
$$

(1.22)

The obtained values of F_i^j and V_i^j are used in (1.21) during the next loop, instead of F_{i-1}^j and V_{i-1}^j, to recalculate the coefficients A_j, B_j, C_j and D_j, and the process of solving (1.20) and (1.22) is repeated. At each station ξ_i we perform 20–25 iterations.

The initial step in the ξ direction is 0.005 but this is reduced to 0.0002 whenever the skin friction τ becomes as small as 0.03. When the step in ξ is reduced, the number of iterations required for each value of ξ increases.

A potential weak point of this scheme is the impossibility of using a variable step across the boundary layer, in the η direction. The "box method" [14] allows such variations, but requires calculating (and storing) the Jacobi matrix for (1.12)–(1.13), which in the case of double-precision calculations can present large storage difficulties.

Anna Dostovalova, The University of Adelaide

1.4   Summary of thin-airfoil theory

Elements of thin-airfoil theory summarized in this section are needed for interpretation of computation results.

1.4.1   Thin-airfoil solution

Let the top and the bottom surfaces of the airfoil be described by

$$y = f_C(x) \pm f_T(x), \qquad 0 \le x \le c. \tag{1.23}$$

where $f_T(0) = f_T(c) = 0$ and $f_C(x)$ is bounded together with its derivative.

First consider the case when $f_T(x)$ is of the form:

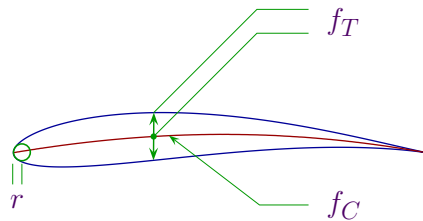$$f_T(x) = (2r)^{1/2}(x^{1/2} + O(x^{3/2})). \tag{1.24}$$

Figure 1.3: Camber and thickness functions

This form of $f_T(x)$ implies that the radius of curvature at the leading edge is r and the shape of the airfoil's nose can be represented in a small neighbourhood by the parabola $y^2 = 2rx$.

If we rotate the airfoil by an angle α as shown, the parametrization of the airfoil's surface becomes

$$x(\xi) + iy(\xi) = [\xi + i(f_C(\xi) \pm f_T(\xi))]e^{-i\alpha}$$
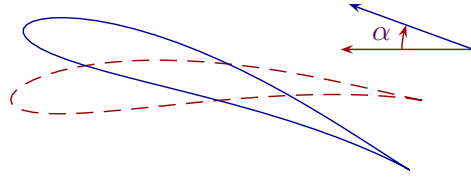
Figure 1.4: Rotating the airfoil

Or,

$$x(\xi) = \xi \cos \alpha + (f_C(\xi) \pm f_T(\xi)) \sin \alpha,$$
$$y(\xi) = -\xi \sin \alpha + (f_C(\xi) \pm f_T(\xi)) \cos \alpha \tag{1.25}$$

Suppose now that r in (1.24) is small and α, $f_C(\xi)$ and $f_C'(\xi)$ have the order of magnitude $O(\sqrt{r})$.

Linearize (1.25) with respect to these small values to give

$$x(\xi) = \xi, \qquad y(\xi) = -\xi\alpha + f_C(\xi) \pm f_T(\xi).$$

Rewrite this as

$$y = -\alpha x + f_C(x) \pm f_T(x), \qquad 0 \le x \le c. \tag{1.26}$$

Note that there is freedom in the possible choice of the initial orientation of the airfoil. Turning the airfoil by a small angle of magnitude $O(\sqrt{r})$ will keep the geometrical configuration in the class of thin airfoils but change

$f_C(x)$. We use this freedom to choose the initial orientation for which the value

$$\alpha_0 = \alpha_0[f_C] \equiv \frac{1}{\pi} \int_0^c \frac{f_C'(s)}{[s(c-s)]^{1/2}} ds$$

is zero. To achieve having $\alpha_0[f_C] = 0$ in the thin-airfoil approximation, we first take some orientation for which the camber function $\bar{f}_C(x)$ may have $\alpha_0[\bar{f}_C] \neq 0$. Then we turn the airfoil by $\alpha_0[\bar{f}_C]$ clockwise to obtain

$$f_C(x) = -\alpha_0[\bar{f}_C]x + \bar{f}_C(x) .$$

Since

$$\frac{1}{\pi} \int_0^c \frac{ds}{[s(c-s)]^{1/2}} = 1,$$

$\alpha_0[kx] = k$, the camber function $f_C(x)$ satisfies

$$\alpha_0[f_C(x)] = -\alpha_0[\bar{f}_C] + \alpha_0[\bar{f}_C] = 0.$$

If $\bar{f}_C(x)$ is such that

$$\bar{f}_C(0) = \bar{f}_C(c) = 0, \tag{1.27}$$

then $\alpha_0[\bar{f}_C]$ coincides in the adopted approximation with the ideal angle of attack [1, p. 70]

$$\alpha_i = \alpha_i[\bar{f}_C] \equiv= \frac{1}{2\pi c^2} \int_0^c \bar{f}_C(x) \frac{1 - (2x/c)}{\{(x/c)[1 - (x/c)]\}^{3/2}} dx . \tag{1.28}$$

The integral in (1.28) is divergent and can be written as a conventional improper integral using formal integration by parts:

$$\begin{aligned}
\alpha_i[\bar{f}_C] &= \frac{1}{2\pi c^2} \int_0^c \bar{f}_C(x) \frac{1 - (2x/c)}{\{(x/c)[1 - (x/c)]\}^{3/2}} dx \\
&= -\frac{1}{\pi c} \int_0^c \bar{f}_C(x) \frac{d}{dx} \frac{1}{\{(x/c)[1 - (x/c)]\}^{1/2}} dx
\end{aligned}$$

$$= -\frac{\bar{f}_C(x)}{\pi c\{(x/c)[1 - (x/c)]\}^{1/2}}\bigg|_0^c + \frac{1}{\pi}\int_0^c \frac{\bar{f}_C'(x)}{[x(c-x)]^{1/2}}dx$$

$$= \frac{1}{\pi}\int_0^c \frac{\bar{f}_C'(x)}{[x(c-x)]^{1/2}}dx = \alpha_0[\bar{f}_C].$$

provided that (1.27) holds.

Consider now the flow $\nabla(Ux + \phi)$ past this airfoil. The perturbation potential $\phi(x,y)$ must satisfy the boundary conditions:

$$\phi_y = (U + \phi_x)\,y'(x) \text{ on } y = y(x), \tag{1.29}$$

$$|\nabla\phi(x,y)| \to 0, \text{ as } \sqrt{x^2 + y^2} \to \infty, \tag{1.30}$$

$$+ \text{Kutta–Zhukovskii–Chaplygin condition} \tag{1.31}$$

The condition (1.31) is a requirement that the speed of the flow be finite at the trailing edge but can be interpreted as another boundary condition at infinity needed to specify the coefficient of the logarithmic term in the expansion of the complex velocity potential.

If we use our assumptions about α, f_C, f_T and expand (1.29) near $y = 0$, $x \in (0, c)$, retaining only first order terms, we obtain the boundary condition:

$$\phi_y = U(-\alpha + f_C'(x) \pm f_T'(x)), \qquad y = 0_\pm. \tag{1.32}$$

Combining (1.30), (1.31) and (1.32) with $\nabla^2\phi = 0$ gives the "thin-airfoil" problem. The complex velocity potential $w(z = x + iy)$ for this problem is well-known (e.g. [15]), its derivative is

$$\frac{dw}{dz} = -\frac{U}{\pi i}\sqrt{\frac{z-c}{z}}\int_0^c \sqrt{\frac{s}{c-s}}\frac{(-\alpha + f_C'(s))}{(s-z)}ds - \frac{U}{\pi}\int_0^c \frac{f_T'(s)}{(s-z)}ds. \tag{1.33}$$

Throughout, unless explicitly specified otherwise, we will use the following convention for the branches of the square root:

$$\sqrt{z-b} \equiv |z-b|^{1/2}\exp(i\arg(z-b)/2), \quad \arg(z-b) \in [0, 2\pi). \tag{1.34}$$
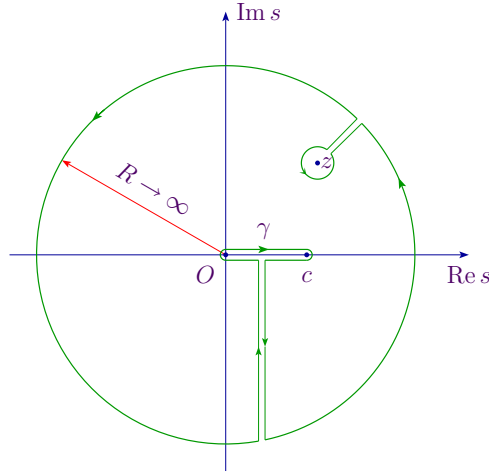
Figure 1.5: Integration paths for formula (1.36)

Also,

$$\sqrt{(z-b)/(z-a)} = \sqrt{(z-b)}/\sqrt{(z-a)}\,.$$

Similarly,

$$(z-b)^r = |z-b|^r \exp\{ir\arg(z-b)\}, \qquad \arg(z-b) \in [0, 2\pi). \qquad (1.35)$$

Solution (1.33) satisfies the Kutta-Zhukovskii-Chaplygin condition provided that

$$f'_T(x) \to 0, \ \text{as } x \to c,$$

quickly enough. We can assume that

$$f'_T(x) \le M \cdot |c-x|^\lambda, \quad (M \text{ and } \lambda \text{ constant and positive}),$$

which will guarantee boundedness of (1.33) at $z = c$. If $f'_T(c) \ne 0$, the last term has a logarithmic singularity at $z = c$. The first term in the right-hand

side of (1.33) is finite at $z = c$, which can be seen from the result

$$2i \int_0^c \sqrt{\frac{s}{c-s}} \frac{1}{s-z} ds = - \int_\gamma \frac{\sqrt{s}}{\sqrt{s-c}(s-z)} ds$$

$$= 2\pi i (1 - \sqrt{z}/\sqrt{z-c}) . \tag{1.36}$$

Formula (1.36) follows from the Cauchy theorem applied to the contour shown in Figure 1.5.

The solution (1.33) fails in the neighbourhood of the leading edge giving infinite velocities. It must be replaced there by a properly matched perturbation term from the inner solution describing a flow past parabola in a uniform stream.

1.4.2 Inner solution

The complex velocity potential of the inner solution is

$$f_{\text{inner}}(z) = rU(Z + W(Z)) \mid_{Z \equiv X + iY = z/r}, \tag{1.37}$$

where $W(Z) = (\beta - i)(2Z - 1)^{1/2}$. Note that, if $y^2 = 2rx$, then

$$W(z/r) = (\beta - i)(y/r + i) = (1 + \beta y/r) + i(\beta - y/r)$$

and $\operatorname{Im} F(z) = rU\beta = \text{const}$, that is the parabola $y^2 = 2rx$ is a streamline.

Differentiation of (1.37) gives the complex velocity:

$$f'_{\text{inner}}(z) = U(1 + W'(Z) \mid_{Z = z/r})$$

where $W'(Z) = (\beta - i)(2Z - 1)^{-1/2}$. On the surface of the parabola $y^2 = 2rx$, the complex velocity is

$$f'_{\text{inner}}(z) = U(1 + (\beta - i)/(i + y/r))$$

$$= U[1 + (\beta - i)/(i \pm \sqrt{2x/r})] \tag{1.38}$$

Anna Dostovalova, The University of Adelaide

1.4.3 Thin-airfoil solution on the airfoil surface

Consider now the solution (1.33) on the surface of the airfoil. The behaviour of $w'(z)$ as $x \to 0_+$ is described on the airfoil's surface by

$$\frac{dw}{dz} = \pm U \left[\alpha \left(\frac{c}{x} \right)^{1/2} - i \left(\frac{r}{2x} \right)^{1/2} \right] + \gamma(x, r), \qquad (1.39)$$

where

$$|\gamma(x, r)| \leq \text{const} \cdot \sqrt{r} \text{ as } x \to 0.$$

The following result is needed for derivation of formula (1.39).

Plemelj–Sokhotski formulae: *If a real function $f(s)$ is smooth on (a, b), $z = x + iy$ and $x \in (a, b)$, then*

$$\lim_{y \to \pm 0} \text{Re} \int_a^b \frac{f(s)}{s - z} ds = \text{p.v.} \int_a^b \frac{f(s)}{s - x} ds \qquad (1.40)$$

$$\lim_{y \to \pm 0} \text{Im} \int_a^b \frac{f(s)}{s - z} = \pm \pi i f(x) \qquad (1.41)$$

The derivation of (1.40) and (1.41) is straightforward, e.g. see [20].

Applying (1.40) and (1.41) to (1.33) we find that, when $x \in (0, c)$ and $y \to 0_\pm$,

$$\phi_x = \pm \frac{U}{\pi} \sqrt{\frac{c - x}{x}} \text{ p.v.} \int_0^c \sqrt{\frac{s}{c - s}} \frac{(-\alpha + f'_C(s))}{(x - s)} ds + \frac{U}{\pi} \text{ p.v.} \int_0^c \frac{f'_T(s)}{x - s} ds$$

$$\phi_y = \pm U(\pm 1)(-\alpha + f'_C(x)) \pm f'_T(x) = U(-\alpha + f'_C(x) \pm f'_T(x)).$$

Here we used the fact that, if $x \in (0, c)$,

$$\lim_{y \to 0_\pm} \sqrt{\frac{z - c}{z}} = \pm i \sqrt{\frac{c - x}{x}} .$$

The expression for ϕ_x can be further simplified if we take into account the fact that

$$\text{p. v.} \int_0^c \sqrt{\frac{s}{c-s}} \frac{ds}{(x-s)} = -\frac{1}{2}\left(-2\pi i \lim_{|z|\to\infty}\left[i\sqrt{z/(z-c)}\right]\right) = -1.$$

Then

$$\phi_x = \pm U\alpha\sqrt{\frac{c-x}{x}} \pm \frac{U}{\pi}\sqrt{\frac{c-x}{x}} \,\text{p. v.} \int_0^c \sqrt{\frac{s}{c-s}}\frac{f'_C(s)}{x-s}ds$$
$$+ \frac{U}{\pi}\,\text{p. v.} \int_0^c \frac{f'_T(s)}{x-s}ds. \tag{1.42}$$

Now consider the behaviour of ϕ_x as $x \to 0_+$. We need to obtain the estimates of some standard integrals as $x \to 0_\pm$.

In order to estimate the last term in (1.42) consider

$$L(x) = \text{p. v.} \int_0^\sigma \frac{ds}{\sqrt{s}(s-x)}$$

where $\sigma > 0$ is small but fixed. Evaluate $L(x)$:

$$L(x) = \frac{1}{\sqrt{x}}\ln\left|\frac{\sqrt{\sigma}+\sqrt{x}}{\sqrt{\sigma}-\sqrt{x}}\right| = O(1), \tag{1.43}$$

since

$$\ln\left|\frac{\sqrt{\sigma}+\sqrt{x}}{\sqrt{\sigma}-\sqrt{x}}\right| = \ln(1+O(\sqrt{x})) = O(\sqrt{x}).$$

The result (1.43) allows us to conclude that the absolute value of the last term in (1.42) is $\leq \text{const} \cdot \sqrt{r}$.

Next consider

$$I(x) = \text{p. v.} \int_0^c \frac{x f'_C(s)}{\sqrt{s(c-s)}(s-x)}ds$$
$$= x\underbrace{\int_0^c \frac{f'_C(s)-f'_C(x)}{\sqrt{s(c-s)}(s-x)}ds}_{\text{abs. value} \leq \text{const.} \sqrt{r}} + x f'_C(x)\,\underbrace{\text{p. v.} \int_0^c \frac{1}{\sqrt{s(c-s)}(s-x)}ds}_{=0}$$
$$= O(x\sqrt{r}). \tag{1.44}$$

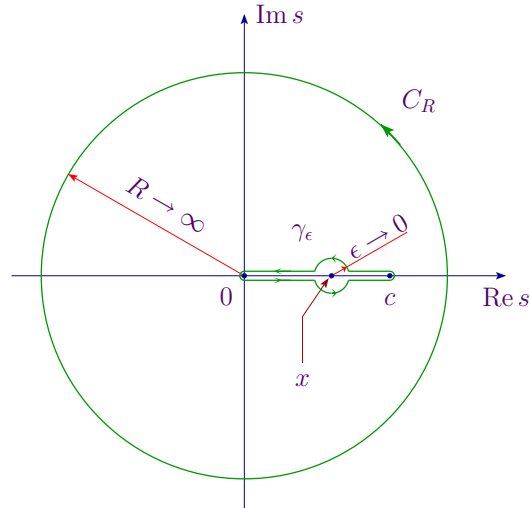Anna Dostovalova, The University of Adelaide

Figure 1.6: Integration paths for formula (1.45)

Here we used the result:

$$J(x, \delta) \equiv \text{p. v.} \int_0^c \frac{ds}{s^\delta (c-s)^{1-\delta}(s-x)} = \frac{\pi \cot(\delta \pi)}{x^\delta (c-x)^{1-\delta}}, \qquad (1.45)$$

provided $x \in (0, c)$ and $\delta \in (0, 1)$. Formula (1.45) can be obtained if we consider

$$0 = \lim_{R \to \infty} \int_{C_R} \frac{ds}{s^\delta (s-c)^{1-\delta}(s-x)} = \lim_{\epsilon \to 0} \int_{\gamma_\epsilon} \frac{ds}{s^\delta (s-c)^{1-\delta}(s-x)}$$

$$= J(x, \delta) \left(e^{i\delta\pi} - e^{-i\delta\pi} \right) - \frac{\pi i \left(e^{i\delta\pi} + e^{-i\delta\pi} \right)}{x^\delta (c-s)^{1-\delta}},$$

where C_R and γ_ϵ are shown in Figure 1.6.

Formula (1.44) allows us to estimate the integral from the second term of (1.42):

$$\int_0^c \sqrt{\frac{s}{c-s}} \frac{f'_C(s)}{x-s} ds = -\int_0^c \frac{f'_C(s) ds}{\sqrt{s(c-s)}} - \underbrace{I(x)}_{=O(x\sqrt{r})} \; .$$

Anna Dostovalova, The University of Adelaide

Thus, in view of $\alpha \sim \sqrt{r}$,

$$U\alpha\sqrt{\frac{c-x}{x}} = U\alpha\sqrt{\frac{c}{x}} + O(\sqrt{rx}),$$

$$\frac{U}{\pi}\sqrt{\frac{c-x}{x}} \,\text{p.v.} \int_0^c \sqrt{\frac{s}{c-s}}\frac{f'_C(s)}{x-s}ds$$

$$= \frac{U}{\pi}\left(\sqrt{\frac{c}{x}} + O(\sqrt{rx})\right)\left(-\underbrace{\int_0^c \frac{f'_C(s)ds}{\sqrt{s(c-s)}}}_{\equiv \pi\alpha_0[f_C]=0} + O(x\sqrt{r})\right)$$

$$= O(\sqrt{xr})\,,$$

$$\frac{U}{\pi}\,\text{p.v.} \int_0^c \frac{f'_T(s)}{x-s}ds = O(\sqrt{r})\,,$$

and formula (1.39) follows.

Matching

The solution near the parabolic leading edge is described by

$$f'_{\text{inner}}(z) = U(1 + (\beta - i)/(i \pm \sqrt{2x/r}))\,. \tag{1.46}$$

This solution replaces the thin-airfoil solution

$$f'_{\text{outer}}(z) = U \pm U\left[\alpha\sqrt{\frac{c}{x}} - i\sqrt{\frac{r}{2x}}\right] + O(r^{1/2})\,. \tag{1.47}$$

at distances $\sim r$ from the leading edge.

To make the solutions match, we compare them in some intermediate region, e.g. taking $x \sim r^{1-\delta}$ $(0 < \delta < 1)$, we find that the two solutions match if

$$\beta = \alpha(2c/r)^{1/2}\,. \tag{1.48}$$

Result (1.48) appeared in this explicit form in [33]; its equivalent form was established earlier in [25].

Anna Dostovalova, The University of Adelaide

Note. We can use more general assumptions on the intermediate region. Let $x \sim r\sigma(r)$ where

$$\sigma(r) \to \infty \quad \text{as } r \to 0, \tag{1.49}$$

and

$$r\sigma(r) \to 0 \quad \text{as } r \to 0. \tag{1.50}$$

Condition (1.49) guarantees that $x \gg r$, whereas condition (1.50) gives $x \ll c$ ($c = O(1)$). Verifying that the terms in the square brackets in (1.47) are dominant over $O(r^{1/2})$

$$\frac{1}{\sqrt{r}} \left[\alpha \sqrt{\frac{c}{x}} - i \sqrt{\frac{r}{2x}} \right] = \frac{1}{\sqrt{r}} \left[\alpha \sqrt{\frac{c}{r}} \frac{1}{\sqrt{\sigma(r)}} - i \frac{1}{\sqrt{2\sigma(r)}} \right]$$

$$= \underbrace{[\alpha \sqrt{c/r} - i/\sqrt{2}]}_{O(1)} \frac{1}{\sqrt{r\sigma(r)}} \to \infty \quad \text{as } r \to 0,$$

we obtain the same combination of principal terms and hence the same relationship between β and α.

1.5 Parabolic solution

Computation of a boundary-layer flow first requires the solution of the inviscid problem to be known, so providing the input $u_e(s)$ or $\sigma^p(\xi)$. In the case of a parabola, such a solution can be found immediately using conformal mapping. As this is a well-known result, we describe it here only briefly.

Consider a body with a parabolic surface in a uniform stream of incompressible fluid. As in Section 1.2 we use spatial variables scaled to the radius of curvature of the leading edge. We map the flow region exterior to that
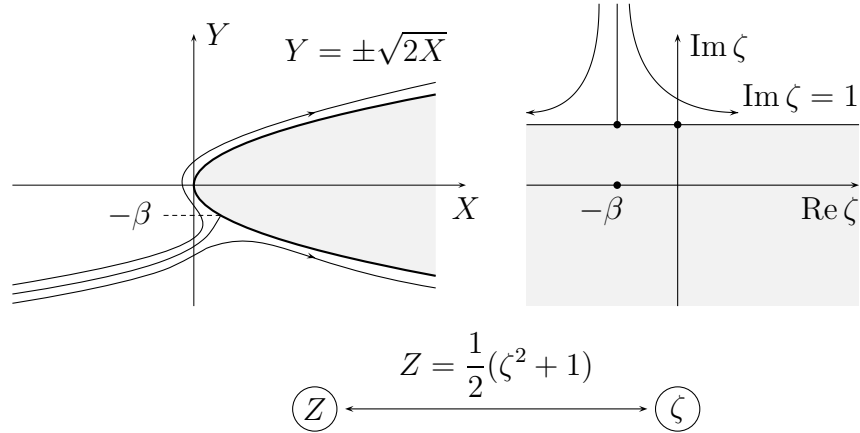
Figure 1.7: Sketch of a parabola at angle of attack.

parabola in the $Z = X + iY$ plane onto the region $\text{Im}\,\zeta \geq 1$ of a ζ-plane by

$$Z = \frac{1}{2}(\zeta^2 + 1). \tag{1.51}$$

It is easy to check that the horizontal line $\text{Im}\,\zeta = 1$ maps to the parabola $Y = \pm\sqrt{2X}$.

The complex velocity potential f is now taken as

$$f = \frac{1}{2}(\zeta + \beta - i)^2, \tag{1.52}$$

which gives a simple stagnation-point flow in the ζ-plane with the line $\text{Im}\,\zeta = 1$ as a streamline and a stagnation point at $\zeta = -\beta + i$. In combination with (1.51), the potential (1.52) behaves as a unit stream $f \to Z$ in the Z-plane at infinity. Now $|df/dZ| = |(df/d\zeta)/(dZ/d\zeta)|$ gives the required velocity input u_{e} to the boundary layer equations. The parameter β determines the position of the stagnation point on the parabola, with symmetric flow for $\beta = 0$, but with the stagnation point in $Y < 0$ if $\beta > 0$.

The results of Werle and Davis [36] show that the laminar boundary layer on the upper surface of the parabola remains unseparated for all

$$\beta < \beta_0 \approx 1.156.$$

We have confirmed this boundary-layer computation using our own program as described in Section 1.3.

The derivative of the formula (1.52) is used to construct the complex velocity near the leading edge in the $z = x + iy$ plane, namely (restoring dimensions)

$$f'_{\text{inner}}(z) = U(1 + (\beta - i)/\sqrt{2(z/r) - 1}). \tag{1.53}$$

In particular, if $y = \pm\sqrt{2rx}$, then

$$f'_{\text{inner}}(z) = U(1 + (\beta - i)/(i \pm \sqrt{2x/r})) \tag{1.54}$$

The parameter β must be chosen so that $f'_{\text{inner}}(z)$ matches a thin-airfoil complex velocity $f'_{\text{outer}}(z)$ (see, for example, [33]), which describes the flow at distances much greater than r from the leading edge.

The behaviour of this thin-airfoil velocity $f'_{\text{outer}}(z)$ as $x \to 0_+$, $y \to 0_\pm$ on the airfoil's surface is given by

$$f'_{\text{outer}}(z) = U \pm U\left[\alpha\sqrt{\frac{c}{x}} - i\sqrt{\frac{r}{2x}}\right] + O(r^{1/2}). \tag{1.55}$$

If we compare (1.54) and (1.55) in an intermediate region $r \ll x \ll c$, we can see that the principal terms coincide if

$$\beta = \alpha\sqrt{\frac{2c}{r}} \tag{1.56}$$

(see [25] and [33] for more details about this formula). If we add to f'_{inner} given by (1.53) a function of $Z = z/r$ that is analytic in the flow domain

and decays faster than $O(Z^{-1/2})$ when $|Z| \to \infty$, matching gives the same formula (1.56), because this function has no influence on the leading terms in the intermediate region. Hence the relationship (1.56) between the parameter β and α can be used for some non-parabolic noses.

Thus for parabolas the range of angle of attack for unseparated flow is given by

$$\alpha < \left(\frac{\beta_0}{\sqrt{2}}\right)\sqrt{\frac{r}{c}} \tag{1.57}$$

or

$$\alpha < 0.818\sqrt{\frac{r}{c}}. \tag{1.58}$$

Our aim now is to increase the number 0.818 in (1.58) by nose shape modification; that is, to increase the value of β_0 above the parabola value 1.156.

1.6 Family of nose shapes

To generalise to non-parabolic shapes, suppose that we modify the relation (1.51) between Z and ζ so that at infinity we still approach the parabola, but near the nose achieve a distortion. Consider for example the following 5-parameter family of mappings

$$Z = \frac{1}{2}(\zeta^2 + 1) + \frac{1}{1 - ih\zeta} \cdot \frac{p + iq}{\zeta - (a + ib)}. \tag{1.59}$$

where p, q, a, b, h are given real parameters. Note that we have introduced singularities at $\zeta = a + ib$ and $\zeta = -i/h$; hence it is necessary that $b < 1$ and $h > -1$ to keep this singularity out of the field of flow $\operatorname{Im}\zeta \geq 1$. The same complex velocity potential f given by (1.52) as a function of ζ can still be used; in particular, note that the resulting complex velocity has the form of (1.53) plus a suitable correction, as required.
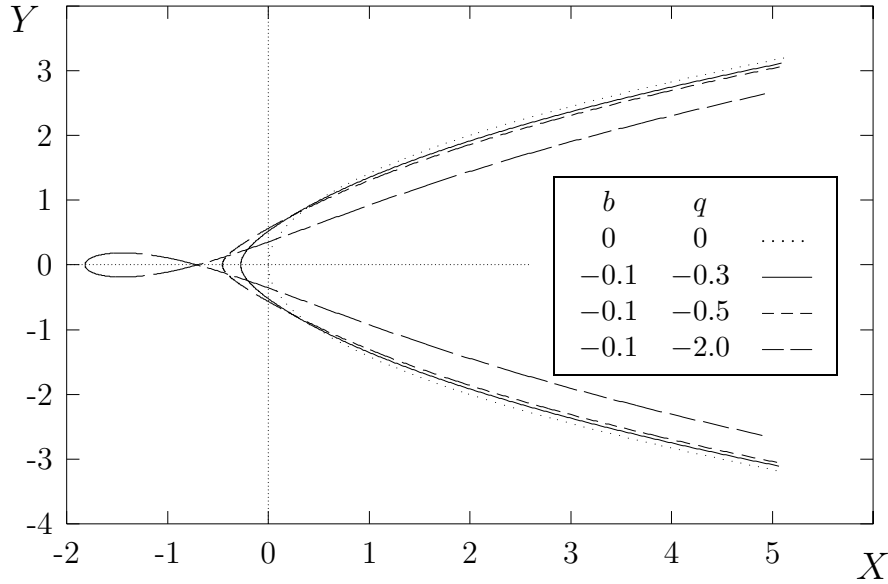
Figure 1.8: Examples of symmetrical shapes.

Firstly, let us consider the special case $h = 0$. We can distinguish between (vertically) symmetric and non-symmetric noses. In particular, the body shape can be written in parametric form (setting $\zeta = t + i$)

$$
\begin{cases}
X = \dfrac{1}{2}t^2 + \dfrac{p(t-a) + q(1-b)}{(t-a)^2 + (1-b)^2} \\[2mm]
Y = t + \dfrac{q(t-a) - p(1-b)}{(t-a)^2 + (1-b)^2}\,.
\end{cases}
\tag{1.60}
$$

In effect, the parametric system (1.60) defines the nose shape functions $g_{\pm}(x/r)$ of equation (1.2) introduced in Section 1. Letting $a = p = 0$ in (1.60) we have

$$
\begin{cases}
X = \dfrac{1}{2}t^2 + \dfrac{q(1-b)}{t^2 + (1-b)^2} \\[2mm]
Y = t + \dfrac{qt}{t^2 + (1-b)^2}.
\end{cases}
\tag{1.61}
$$

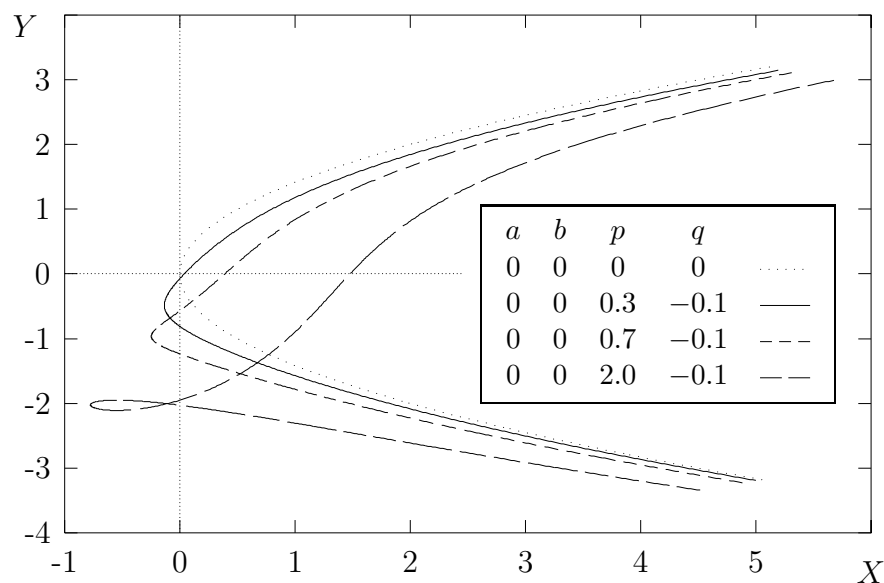| a	b	p	q	
0	0	0	0	....
0	0	0.3	-0.1	————
0	0	0.7	-0.1	- - - -
0	0	2.0	-0.1	— — —

Figure 1.9: Examples of non-symmetrical shapes.

The relation (1.61) gives noses which are symmetric with respect to the X-axis. For any point (X, Y) corresponding to parameter value t, there is also a point with coordinates $(X, -Y)$ corresponding to parameter value $-t$. Figure 1.8 shows some examples of this type of symmetric nose. Note that geometrically feasible shapes must have $q < 0$, and also q cannot be too negative; the self-intersecting shape for $q = -2$ shown in Figure 1.8 is not feasible.

If a or p are non-zero, (1.60) describes an unsymmetrical nose. In particular, if p is positive, the nose bends downward, i.e. is "drooped". Figure 1.9 shows some examples of this type; again there are limits on p and q for geometrically feasible shapes. Figure 1.9 includes an example of a self-intersecting unsymmetrical shape.

We now discuss results of searches for improved nose shapes, for reasonably small distortions of the parabola. Note that some extreme shapes shown in Figures 1.8 and 1.9 will not be acceptable from the boundary-layer separation point of view, even though they are geometrically feasible.

1.7 Numerical results
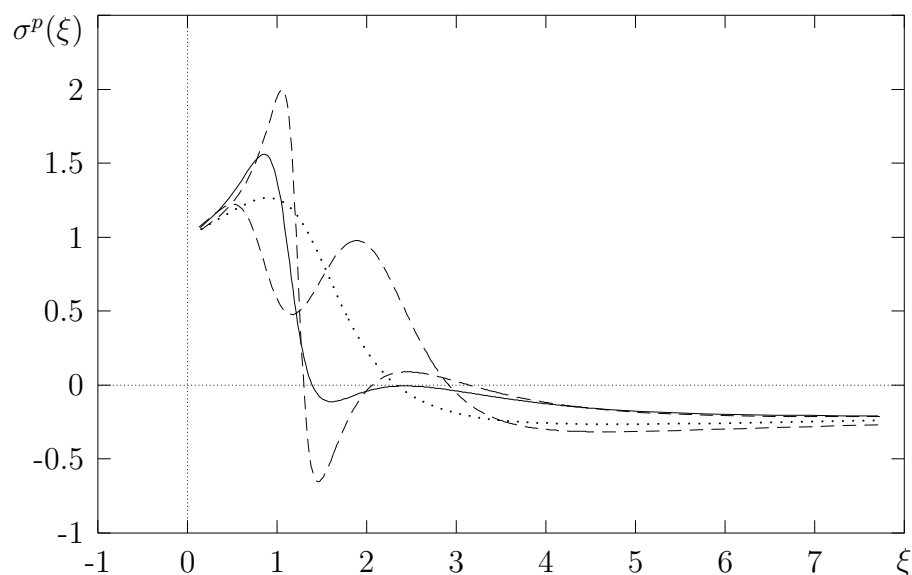
Figure 1.10: Examples of $\sigma^p(\xi)$ for different sets of parameters a, b, p and q compared with $\sigma^p_{\mathrm{parab}}(\xi)$ (dotted line) for $\beta = 1.156$.

As we can see from (1.12)–(1.13), the only input that depends on the geometry of the problem and, therefore, on the parameters a, b, p, q in (1.59), is the pressure gradient function $\sigma^p(\xi)$. It would be expedient to be able to use this function alone for making decisions in favour of, or against, one or

another combination of these parameters, without the necessity of solving the boundary-layer equations every time. Comparison of the behaviour of $\sigma^p(\xi)$ with the corresponding behaviour of the boundary layer obtained in numerical trials with different values of the parameters shows that the following mnemonic rule can be used for making a favorable decision. Taking $\sigma^p(\xi)$ for a parabola $(= \sigma^p_{\text{parab}}(\xi))$ with maximum value of β $(= 1.156)$ as a reference we consider a set of values a, b, p and q to be a "good" choice if (a) the plot of the resulting curve $\sigma^p(\xi)$ for the same value of β lies above $\sigma^p_{\text{parab}}(\xi)$ after the second intersection, and (b) the local minimum of $\sigma^p(\xi)$ is not lower than the local minimum of $\sigma^p_{\text{parab}}(\xi)$. Condition (b) is needed to avoid an early crisis, whereas condition (a) indicates delayed boundary-layer separation.

Figure 1.10 illustrates this rule. The plot of $\sigma^p_{\text{parab}}(\xi)$ is a dotted line. Acceptable $\sigma^p(\xi)$ is shown with a solid line. Dashed lines are examples of $\sigma^p(\xi)$ which do not satisfy either condition (a) or condition (b).

After a, b, p and q have been chosen, we carry out actual boundary-layer computations, gradually increasing β until separation of the boundary layer occurs. The resulting value of β is used for generating the pressure gradient function $\sigma^p(\xi)$ which is then used as a new reference for the subsequent step of optimisation. Use of this rule allows us to reduce significantly the time required for obtaining the optimal set of parameters.

Our boundary-layer computations showed that it was possible by careful choice of a, b, p and q to increase the critical value β_0 of the angle-of-attack parameter β, thereby delaying laminar separation. Although there are non-trivial optimal choices of some parameters, the increase in β_0 depends to a certain extent on how far the modified shape can be allowed to deviate from
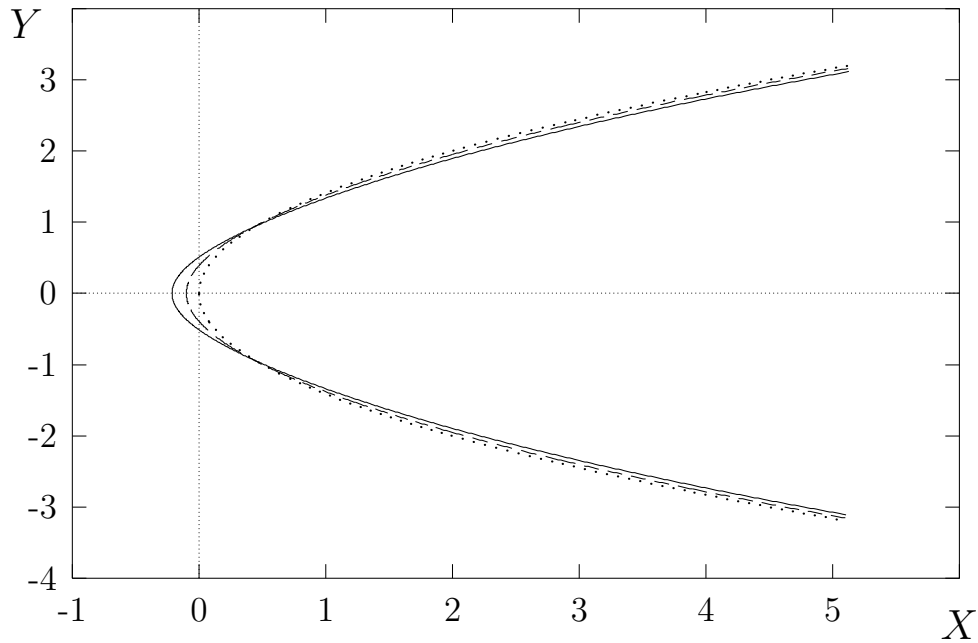
Line style	a	b	p	q	h	β_0
$\cdots\cdots\cdots$	0	0	0	0	0	1.156
$-----$	0	-0.6	0	-0.2	0.25	1.210
————	0	-0.8	0	-0.5	0.3	1.269

Figure 1.11: A sequence of symmetrical noses with increasing β_0

the parabola.

If we wish to ease requirements on smallness of r, we should consider shapes which approach the asymptotic parabola as quickly as possible downstream. In this sense with $h = 0$, the perturbation term in (1.59) is $O(\zeta^{-1})$ and is not a particularly good choice, as the resulting shape becomes parabolic only at considerable distances from the nose. On the other hand, the full expression (1.59) with $h > 0$ allows us to achieve a better control as we

increase β_0, with the shape changes remaining local to the nose, because for $h > 0$, the perturbation to the parabola decays like ζ^{-2} as $\zeta \to \infty$. The parameter h in the first factor of the perturbation term is used to vary the shape, small real positive values of h being used in order to confine its effect to the far field. The shapes with $a = p = 0$ are still symmetrical.

Figure 1.11 and Figure 1.12 show sequences of (respectively) symmetrical
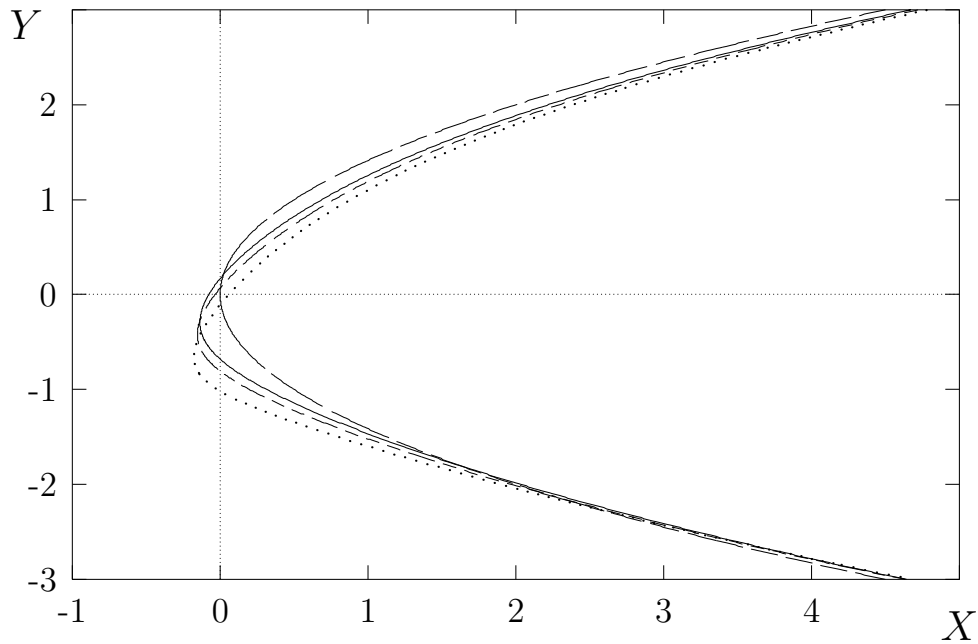
Line style	a	b	p	q	h	β_0
—— ——	0	0	0	0	0	1.156
————	−0.2	−0.4	0.27	−0.27	0.3	1.252
− − − − −	−0.2	−0.4	0.4	−0.29	0.25	1.270
· · · · · · · · · ·	−0.4	−0.4	0.6	−0.4	0.25	1.289

Figure 1.12: A sequence of non-symmetrical noses with increasing β_0.

Anna Dostovalova, The University of Adelaide

and non-symmetrical noses with increasing β_0. We can see that in the case of non-symmetrical noses the larger β_0 values are obtained by increasing the distortions, especially on the upper surface.

1.8   Conclusion

Our analysis suggests airfoil nose shapes which delay separation of the laminar boundary layer on the upper surface of the airfoil. Each optimisation result is valid in a class of thin airfoils with the same apparent leading edge curvature radius r, assumed to be small compared to the chord. Symmetric modifications, essentially just by sharpening the nose, can improve the result for a parabolic nose ($\alpha < 0.818\sqrt{r/c}$) to at least $\alpha < 0.897\sqrt{r/c}$. We also showed that further improvement is possible for unsymmetrical noses, and gave an example of a realistic "drooped" nose with $\alpha_0 = 0.912\sqrt{r/c}$.

Chapter 2

Generally shaped finite-length airfoils

2.1 Introduction

In Chapter 1 we were concerned with the boundary layer computation near leading edges of thin airfoils. Assumptions of the thin-airfoil theory allowed us to approximate the inviscid flow near the leading edge with a flow past an apparent parabola. The resulting pressure coefficient $\sigma^p(\xi)$ had a relatively simple form, as we were able to use explicit formulae for the conformal mapping to yield the potential flow solution. The computational procedure in the case of general airfoils is less straightforward, even though the program developed for the determination of the skin friction requires only minor modifications.

The inviscid flow past a general airfoil can be obtained using conformal mapping of the outer-airfoil region onto the exterior of a standard domain

(usually a disc) for which an analytic form of the solution is known. There are cases when this approach leads to exact solutions (flows past the Zhukovskii profiles, Karman-Trefftz profiles or some simple polygonal airfoils) but commonly the solution is approximate in the sense that it describes an exact flow past a shape approximating the airfoil. When, for example, the Schwarz-Christoffel transformation is used [19] such a shape is a polygon to which the wing section is reduced. If the ideal flow solution is needed for boundary-layer computation, then, in addition to closely fitting the airfoil, the approximating shape must preserve its smoothness properties. This requirement stems from the fact that the boundary-layer separation algorithms are sensitive to singularities of the boundary, or, in physical terms, to fast changes in the pressure gradient, and it is necessary to avoid false predictions of separation from corners which are in fact numerical artefacts.

The Theodorsen-Naiman technique [31, 32, 21, 22, 1] allows us to explicitly construct a mapping that meets such a requirement for a wide class of airfoils. We have developed and describe here a tool that implements this procedure in MATLAB. Simplicity of coding and flexibility in handling graphics and mathematics make MATLAB one of the most suitable environments for such algorithms.

In Section 2.2 we provide a concise and self-contained theoretical background of the method. In Section 2.3, a summary and details of how we implement the technique are given. We also discuss limitations of the method. One of the limitations is the requirement that the near-circle obtained from the airfoil by an auxiliary Zhukovskii mapping must be a star-shaped region. Another limitation is connected with the restriction on the geometry of the trailing edge, which must be a cusp of the first kind. Violation of this restric-

tion may destroy a one-to-one correspondence between angular parameters in the circle and the near-circle planes and result in an inability to satisfy the Kutta-Zhukovskii condition. The trailing-edge geometry limitation is not present if a preliminary Karman-Trefftz transformation is used for mapping to a near-circle plane. Section 2.5 outlines features of the graphical user interface.

2.2 Ideal flow past general airfoils

We will use a methodology developed and published in [31, 32, 21, 22, 1]. Specifics of our procedure require notational adjustments and the theoretical material below is intended to provide this.

Suppose that an airfoil contour is given in the ζ-plane. One of our goals will be to find a transformation $z(\zeta)$, or equivalently $\zeta(z)$, that satisfies

$$\zeta(z) = ze^{i\alpha_1} + O(1) \quad \text{as } |z| \to \infty, \tag{2.1}$$

for some α_1 and conformally maps the exterior of the airfoil onto the exterior of a circle $|z| < R$. The flow past such a circle is described by the complex velocity potential

$$w(z; U_\infty, \alpha_0, R, \Gamma) = U_\infty \left(ze^{-i\alpha_0} + \frac{R^2 e^{i\alpha_0}}{z} \right) + \frac{i\Gamma}{2\pi} \log \frac{ze^{-i\alpha_0}}{R} . \tag{2.2}$$

The condition (2.1) preserves uniformity of the stream at infinity, so the complex velocity potential for the flow in the plane of the airfoil has the form

$$f(\zeta) = w(z(\zeta)) \equiv w(z(\zeta); U_\infty, \alpha_0, R, \Gamma), \tag{2.3}$$

To determine appropriate values of the parameters U_∞, α_0 and Γ in (2.2), consider the complex velocity

$$f'(\zeta) = \frac{w'(z(\zeta))}{\zeta'(z)} = U_\infty e^{-i(\alpha_1+\alpha_0)} + \frac{i\Gamma}{2\pi}\zeta^{-1} + O(\zeta^{-2}). \qquad (2.4)$$

If α is the uniform flow direction angle in the ζ-plane, then we must choose $\alpha_0 = \alpha - \alpha_1$. Parameter U_∞ must be set to the magnitude of the uniform flow at infinity. Similarly, formula (2.4) shows that the circulation Γ of the flow in the z-plane coincides with the circulation of the flow in the physical ζ-plane. Choice of this parameter's value is decided by the Kutta-Zhukovskii condition, and will be discussed later.

The required mapping $z(\zeta)$ can be obtained in three steps.

1) First the Zhukovskii transformation

$$\zeta = \tilde{z} + \frac{a^2}{\tilde{z}} \qquad (2.5)$$

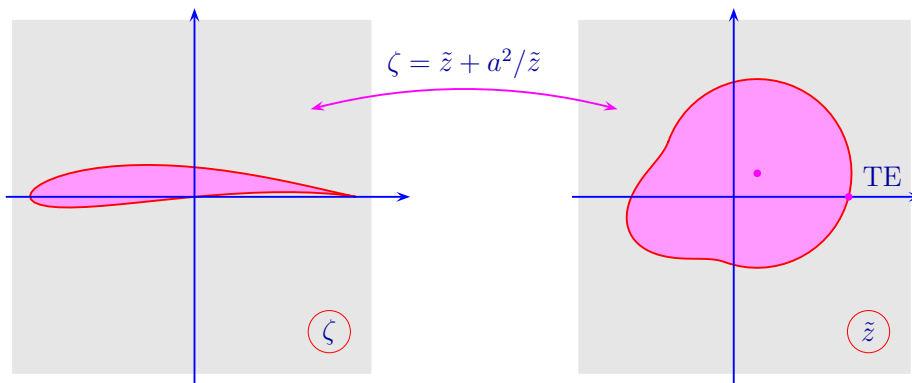maps the flow domain onto a domain in an auxiliary $\tilde{z}$-plane.

Figure 2.1: Zhukovskii mapping

Anna Dostovalova, The University of Adelaide

As a result of this transformation, a cusped part of the boundary is mapped onto a smooth segment, and the trailing edge singularity is removed. Mapping (2.5) also turns an oblong shape that the airfoil commonly has onto a rounded domain which is referred to as a *near-circle* [1].

By changing to a new variable

$$\bar{z} = (\tilde{z} - \varepsilon)e^{-i\alpha_1}, \qquad (2.6)$$

or, equivalently, translating and rotating the coordinate system, we make its origin coincide with the "center" of the near-circle and its positive real axis intersect the image of the trailing edge. This transformation is needed for computational convenience.

2) The second step is to map near-circles to true circles, that is, to apply the mapping

$$\bar{z} = z \exp\{\omega(z)\} , \qquad (2.7)$$

where $\omega(z) = \omega(z; R)$ is analytic if $|z| > R$ and $\omega(z) \to 0$ as $|z| \to \infty$. This form of relation between z and $\bar{z}$ and properties of mapping (2.5) guarantee that the condition (2.1) is met.

3) Combining the first two steps we obtain the composite mapping $\zeta = \zeta(\bar{z}(z))$ and the ideal flow past the airfoil.

There is a certain degree of freedom in the choice of auxiliary parameters a and ε and we use this freedom to improve convergence of the scheme. These parameters cannot be chosen arbitrarily however.

Suppose the chord length of the airfoil is L and let a be a little less than $L/4$. Position the airfoil so that the two conditions are satisfied:

a) the trailing edge is at $\zeta = 2a$,
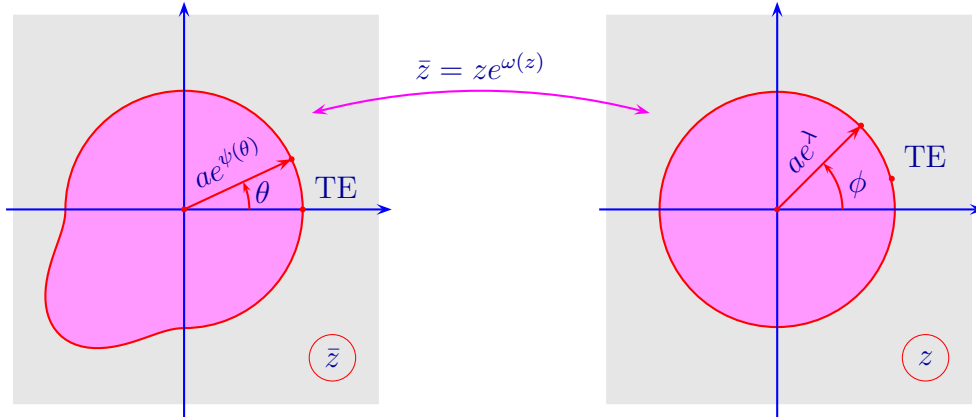
b) the point $\zeta = -2a$ is inside the airfoil.

Figure 2.2: Correspondence between the boundary points

Let θ and ϕ be polar angles in the $\bar{z}$- and z-planes respectively. The boundaries of the near-circle in the $\bar{z}$ plane and its image in the z-plane can be represented as

$$\bar{z} = ae^{\psi(\theta)+i\theta} \quad \text{and} \quad z = ae^{\lambda+i\phi}. \tag{2.8}$$

Here $\psi(\theta)$ is a known function, which we determine from (2.5) and (2.6). If $\zeta = \zeta(t)$ is a given parametric form of the airfoil, then $\bar{z}(t)$ found from (2.5) and (2.6) is a parametrization of the near-circle. Determine $t(\theta)$ from the equation $\arg[\bar{z}(t)] = \theta$ and write

$$ae^{\psi(\theta)} = |\bar{z}(t(\theta))| \quad \Rightarrow \quad \psi(\theta) = \log(|\bar{z}(t(\theta))|/a). \tag{2.9}$$

Note that λ is a constant yet to be chosen, and $R = ae^{\lambda}$.

Correspondence under the mapping (2.7) between the boundary points of the $\bar{z}$ and z domains may be expressed in terms of the dependence $\theta = \theta(\phi)$, for which we must have

$$ae^{\psi(\theta(\phi))+i\theta(\phi)} = ae^{\lambda+i\phi+\omega(ae^{\lambda+i\phi})} \ . \tag{2.10}$$

It turns out that knowledge of $\theta(\phi)$ allows us to determine $\omega(z)$. By (2.10) we have

$$\text{Re}\,\omega(ae^{\lambda+i\phi}) = \psi(\theta(\phi)) - \lambda \ , \tag{2.11}$$

$$\text{Im}\,\omega(ae^{\lambda+i\phi}) = \theta(\phi) - \phi \ . \tag{2.12}$$

Use (2.11) and the Schwarz formula to obtain

$$\text{Re}\,\omega(z) = \frac{1}{2\pi} \int_0^{2\pi} \text{Re}\left[\frac{z + ae^{\lambda+i\varphi}}{z - ae^{\lambda+i\varphi}}\right] (\psi(\theta(\varphi)) - \lambda)d\varphi \ .$$

Hence

$$\omega(z) = \frac{1}{2\pi} \int_0^{2\pi} \frac{z + ae^{\lambda+i\varphi}}{z - ae^{\lambda+i\varphi}} (\psi(\theta(\varphi)) - \lambda)d\varphi + iC \ , \tag{2.13}$$

where C is a real constant. Since we wish to have $\omega(z) \to 0$ as $|z| \to \infty$ we have to set $C = 0$ and choose λ as

$$\lambda = \frac{1}{2\pi} \int_0^{2\pi} \psi(\theta(\varphi))d\varphi \ . \tag{2.14}$$

In order to satisfy (2.12) we must have
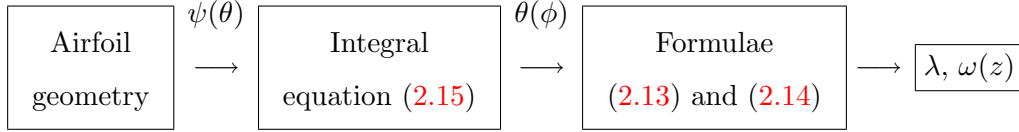
$$\theta(\phi) - \phi = \frac{1}{2\pi}\,\text{p.\,v.} \int_0^{2\pi} \frac{e^{i\phi} + e^{i\varphi}}{e^{i\phi} - e^{i\varphi}} (\psi(\theta(\varphi)) - \lambda)d\varphi \ ,$$

or

$$\theta(\phi) - \phi = \frac{1}{2\pi}\,\text{p.\,v.} \int_0^{2\pi} \cot\left(\frac{\varphi - \phi}{2}\right) \psi(\theta(\varphi))d\varphi \ . \tag{2.15}$$

Anna Dostovalova, The University of Adelaide

Thus, given $\psi(\theta)$, we cannot arbitrarily choose the dependence $\theta(\phi)$ but must use only the solution to (2.15). This leads to the procedure:

$$
\boxed{\begin{array}{c}\text{Airfoil}\\\text{geometry}\end{array}} \xrightarrow{\psi(\theta)} \boxed{\begin{array}{c}\text{Integral}\\\text{equation (2.15)}\end{array}} \xrightarrow{\theta(\phi)} \boxed{\begin{array}{c}\text{Formulae}\\\text{(2.13) and (2.14)}\end{array}} \longrightarrow \boxed{\lambda,\ \omega(z)}
$$

An alternative derivation of (2.15) [31, 32, 1] based on the Laurent series expansion of $\omega(z)$ follows.

Since $\omega(z)$ is analytic in the domain external to the circle $z = Re^{i\phi} = ae^{\lambda + i\phi}$ and vanishes at infinity we can write

$$\omega(z) = \sum_{m=1}^{\infty} (a_m + ib_m)(R/z)^m . \tag{2.16}$$

It follows from (2.10) that

$$\psi - \lambda + i(\theta - \phi) = \sum_{m=1}^{\infty} (a_m + ib_m)(\cos m\phi - i \sin m\phi),$$

and so

$$\psi - \lambda = \sum_{m=1}^{\infty} (a_m \cos m\phi + b_m \sin m\phi), \tag{2.17}$$

$$\theta - \phi = \sum_{m=1}^{\infty} (b_m \cos m\phi - a_m \sin m\phi) . \tag{2.18}$$

It follows from (2.17) that

$$\lambda = a_0 \equiv \frac{1}{2\pi} \int_0^{2\pi} \psi(\theta(\phi)) d\phi, \tag{2.19}$$

$$\begin{Bmatrix} a_m \\ b_m \end{Bmatrix} = \frac{1}{\pi} \int_0^{2\pi} \psi(\theta(\varphi)) \begin{Bmatrix} \cos m\varphi \\ \sin m\varphi \end{Bmatrix} d\varphi . \tag{2.20}$$
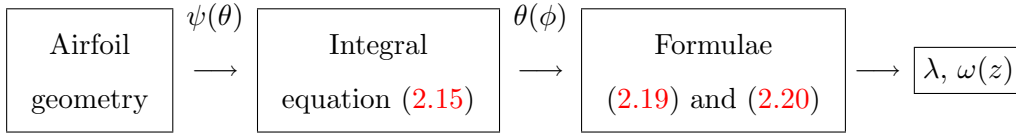
Substitute (2.20) into (2.18)

$$
\theta - \phi = \sum_{m=1}^{\infty} \frac{1}{\pi} \int_0^{2\pi} \psi(\theta(\varphi)) \sin(m(\varphi - \phi)) d\varphi
$$

$$
= \lim_{M \to \infty} \frac{1}{\pi} \int_0^{2\pi} \psi(\theta(\varphi)) \sum_{m=1}^{M} \sin(m(\varphi - \phi)) d\varphi
$$

$$
= \lim_{M \to \infty} \frac{1}{\pi} \int_0^{2\pi} \psi(\theta(\varphi)) \frac{\cos\left((\varphi - \phi)/2\right) - \cos\left((M + 1/2)(\varphi - \phi)\right)}{2 \sin\left((\varphi - \phi)/2\right)} d\varphi .
$$

Using a power series expansion of $\psi(\theta(\varphi))$ at $\varphi = \phi$ and the Riemann-Lebesgue lemma we obtain

$$
\lim_{M \to \infty} \text{p. v.} \int_0^{2\pi} \psi(\theta(\varphi)) \frac{\cos((M + 1/2)(\varphi - \phi))}{\sin((\varphi - \phi)/2)} d\varphi = 0,
$$

hence (2.15) follows.

The strategy for constructing $\omega(z)$ can now be represented as

There is a semi-inverse approach when either ψ or θ are specified in terms of ϕ. Expansion into the Fourier series (2.17) or (2.18) gives the coefficients $\{a_m, \ b_m\}$ and therefore λ and $\omega(z)$. However, when such an approach is used, the shape of the airfoil cannot be considered as the problem input, but must be recovered once $\omega(z)$ is found.

We start the next section by reviewing Naiman's method for approximate solution of (2.15). This method is based on the properties of finite trigonometric expansions and uses the series derivation of (2.15) as a prototype.

2.3   Naiman's method

Naiman's method

Consider a function $\Psi(\phi)$ that represents a finite trigonometric series of the form:

$$\Psi(\phi) = A_0 + \sum_{m=1}^{n}(A_m \cos m\phi + B_m \sin m\phi) , \qquad (2.21)$$

where B_n is taken to be zero.

If $\Psi(\phi)$ is given by (2.21), then conditions

$$\Psi(k\pi/n) = \psi_k \qquad k = 0, \ldots, 2n - 1 \qquad (2.22)$$

are equivalent to

$$A_0 = \frac{1}{2n} \sum_{k=0}^{2n-1} \psi_k ,$$

$$A_m = \frac{1}{(1 + \delta_{mn})n} \sum_{k=0}^{2n-1} \psi_k \cos m\frac{k\pi}{n} \qquad (m = 1, \ldots, n) , \qquad (2.23)$$

$$B_m = \frac{1}{n} \sum_{k=0}^{2n-1} \psi_k \sin m\frac{k\pi}{n} \qquad (m = 1, \ldots, n) .$$

Now introduce

$$\epsilon(\phi) \equiv \sum_{m=1}^{n}(A_m \sin m\phi - B_m \cos m\phi)$$

and consider this function at $\phi = k'\pi/n$ $(k' = 0, \ldots, 2n-1)$. It can be shown [22, 1] that

$$\epsilon(\phi = k'\pi/n) = -\frac{1}{n} \sum_{k=0}^{2n-1} \psi_k \sigma(k - k') , \qquad (2.24)$$

where $\sigma(K) \equiv \begin{cases} \cot \frac{K\pi}{2n} , & K \text{ odd,} \\ 0 , & K \text{ even.} \end{cases}$

Anna Dostovalova, The University of Adelaide

Now let $\phi_j \equiv j\pi/n$, $j = 0, \ldots, 2n - 1$, and consider a finite sequence of numbers $\{\theta_k\}$ ($k = 0, \ldots, 2n - 1$) from $[0, 2\pi)$ that satisfies

$$\theta_j - \phi_j = \frac{1}{n} \sum_{k=0}^{2n-1} \psi(\theta_k)\sigma(k - j), \qquad j = 0, \ldots, 2n - 1. \tag{2.25}$$

Let $\psi_j = \psi(\theta_j)$ and use (2.23) to define A_m and B_m and hence

$$\Omega(z) = \sum_{m=1}^{n}(A_m + iB_m)(ae^{A_0}/z)^m .$$

The image of the circle $z = ae^{A_0 + i\phi}$ ($\phi \in [0, 2\pi)$) under such a transformation can be parametrized as

$$\bar{z} = ae^{\psi^\star(\theta) + i\theta} . \tag{2.26}$$

The superscript $\star$ was used here to indicate that in general $\psi^\star(\theta)$ and $\psi(\theta)$ are different functions. Parameters ϕ and θ corresponding to the same point on the circle are connected as

$$\theta = \theta^\star(\phi) \equiv \arg\left[\bar{z}\left(z = ae^{A_0 + i\phi}\right)\right]$$

Rewrite (2.26) as

$$\bar{z} = ze^{\psi^\star(\theta) - A_0 + i(\theta - \phi)} .$$

Using $\bar{z} = z\exp\{\Omega(z)\}$ with $z = ae^{A_0 + i\phi}$ we have

$$\psi^\star(\theta^\star(\phi)) = A_0 + \sum_{m=1}^{n}(A_m \cos m\phi + B_m \sin m\phi), \tag{2.27}$$

$$\theta^\star(\phi) - \phi = \sum_{m=1}^{n}(B_m \cos m\phi - A_m \sin m\phi). \tag{2.28}$$

It follows from (2.27) and the way the coefficients of this finite trigonometric series have been formed that

$$\psi^\star(\theta^\star(\phi_j)) = \psi_j \equiv \psi(\theta_j). \tag{2.29}$$

Furthermore, it follows from (2.24) that

$$\theta^{\star}(\phi_j) - \phi_j \equiv \sum_{m=1}^{n}(B_m \cos m\phi - A_m \sin m\phi) = \frac{1}{n}\sum_{k=0}^{2n-1}\psi_k\sigma(k - j).$$

Since θ_j satisfy

$$\theta_j - \phi_j = \frac{1}{n}\sum_{k=0}^{2n-1}\psi(\theta_k)\sigma(k - j) = \frac{1}{n}\sum_{k=0}^{2n-1}\psi_k\sigma(k - j),$$

we obtain

$$\theta^{\star}(\phi_j) - \phi_j = \theta_j - \phi_j \quad \Rightarrow \quad \theta^{\star}(\phi_j) = \theta_j.$$

This along with (2.29) gives

$$\psi^{\star}(\theta_j) = \psi(\theta_j) \qquad (j = 0, \ldots, 2n - 1).$$

Hence the shape $\bar{z} = a\exp(\psi^{\star}(\theta) + i\theta)$ coincides with the required near-circle $\bar{z} = a\exp(\psi(\theta) + i\theta)$ at $\theta = \theta_j$ $(j = 0, \ldots, 2n - 1)$ thus approximating it. As a result the approximate airfoil will coincide with the given airfoil at points $\zeta(a\exp(\psi(\theta_j) + i\theta_j))$, where $\zeta(\bar{z})$ is defined by (2.5) and (2.6).

If the flow is uniform at infinity with magnitude U_∞ and direction angle α, then its complex velocity potential is

$$f(\zeta) = w(z(\zeta); U_\infty, \alpha_0 \equiv \alpha - \alpha_1, ae^{A_0}, \Gamma).$$

Circulation Γ is chosen so as to satisfy the Kutta-Zhukovskii condition (also referred to as the Chaplygin condition [15, 16]):

> for $f'(\zeta)$ to be finite at the trailing edge, where $\zeta'(z) = 0$, the rear stagnation point of the z-flow must correspond to the trailing edge of the airfoil.

Suppose that $z_T = ae^{A_0 + i\phi_T}$ is a point corresponding to the trailing edge $\zeta = 2a$. Then we must have:

$$U_\infty \left(e^{-i\alpha_0} - \frac{a^2 e^{2A_0 + i\alpha_0}}{a^2 e^{2A_0 + i2\phi_T}} \right) + \frac{i\Gamma}{2\pi} \frac{1}{ae^{A_0 + i\phi_T}} = 0,$$

or

$$\Gamma = 4\pi ae^{A_0} U_\infty \sin(\alpha_0 - \phi_T) = 4\pi ae^{A_0} U_\infty \sin(\alpha - \alpha_1 - \phi_T). \qquad (2.30)$$

The angle ϕ_T in (2.30) is found from the equation:

$$\phi + \sum_{m=1}^{n} (B_m \cos m\phi - A_m \sin m\phi) = 0. \qquad (2.31)$$

Review of properties of finite trigonometric series

The following properties of Dirichlet's kernels will be often used:

$$S_n = \sum_{k=1}^{n} \cos kx = \frac{\sin(n+1/2)x - \sin x/2}{2\sin x/2} \; ; \qquad (2.32)$$

$$D_n = \sum_{k=1}^{n} \sin kx = \frac{\cos x/2 - \cos(n+1/2)x}{2\sin x/2} \; . \qquad (2.33)$$

Given $B_n = 0$ consider

$$\Psi(\phi) = A_0 + \sum_{m=1}^{n} (A_m \cos m\phi + B_m \sin m\phi) . \qquad (2.34)$$

If $\psi_k = \Psi(k\pi/n)$ $(k = 0, \ldots, 2n-1)$, then formulae (2.23) hold. Let us verify this.

- Show for A_0:

$$\frac{1}{2n} \sum_{k=0}^{2n-1} \psi_k = \frac{1}{2n} \sum_{k=0}^{2n-1} \left(A_0 + \sum_{m=1}^{n} A_m \cos m\frac{k\pi}{n} + \sum_{m=1}^{n-1} B_m \sin m\frac{k\pi}{n} \right)$$

$$= A_0 + \sum_{m=1}^{n} A_m \underbrace{\sum_{k=0}^{2n-1} \cos k\frac{m\pi}{n}}_{1 + \frac{-\sin(m\pi/2n) - \sin(m\pi/2n)}{2\sin(m\pi/2n)}} + \sum_{m=1}^{n-1} B_m \underbrace{\sum_{k=0}^{2n-1} \sin k\frac{m\pi}{n}}_{\frac{\cos(m\pi/2n) - \cos(-m\pi/2n)}{2\sin(m\pi/2n)}}$$

$$= A_0 + 0 + 0 = A_0.$$

- Show for A_m $(m = 1, \ldots, n - 1)$:

$$\frac{1}{n} \sum_{k=0}^{2n-1} \psi_k \cos k\frac{k\pi}{n} = \frac{1}{n} \sum_{k=0}^{2n-1} \left(A_0 \cos m\frac{k\pi}{n} + \sum_{j=1}^{n} A_j \cos j\frac{k\pi}{n} \cos m\frac{k\pi}{n} \right.$$

$$\left. + \sum_{j=1}^{n-1} B_j \sin j\frac{k\pi}{n} \cos m\frac{k\pi}{n} \right) .$$

We have

$$\sum_{k=0}^{2n-1} A_0 \cos k\frac{m\pi}{n} = 0 \qquad \text{(shown above);} \qquad (2.35)$$

and

$$\sum_{k=0}^{2n-1} \cos k\frac{j\pi}{n} \cos k\frac{m\pi}{n} = \frac{1}{2} \sum_{k=0}^{2n-1} \cos k\frac{(j-m)\pi}{n} + \frac{1}{2} \sum_{k=0}^{2n-1} \cos k\frac{(j+m)\pi}{n}$$

$$= \begin{cases} 0, & j \neq m \\ \frac{1}{2} \cdot 2n = n, & j = m \end{cases}$$

(as $j \pm m$ is integer and $|j + m| < 2n$ formula (2.32) can be applied if $j \neq m$). Hence

$$\frac{1}{n} \sum_{k=0}^{2n-1} \sum_{j=1}^{n} A_j \cos j\frac{k\pi}{n} \cos m\frac{k\pi}{n} = \frac{1}{n} A_m \sum_{k=0}^{2n-1} \cos m\frac{k\pi}{n} \cos m\frac{k\pi}{n}$$

$$= \frac{1}{n} A_m n = A_m. \qquad (2.36)$$

Evaluate the coefficient of B_j:

$$\sum_{k=0}^{2n-1} \sin k\frac{j\pi}{n} \cos k\frac{m\pi}{n} = \sum_{k=0}^{2n-1} \frac{1}{2} \left(\sin k\frac{(j+m)\pi}{n} + \sin k\frac{(j-m)\pi}{n} \right) = 0 \quad (2.37)$$

since, if integer $\ell \neq 0$ and $|\ell| < 2n$,

$$\sum_{k=0}^{2n-1} \sin k\frac{\ell\pi}{n} = \frac{\cos \frac{\ell\pi}{2n} - \cos\left(-\frac{\ell\pi}{2n}\right)}{2 \sin \frac{\ell\pi}{2n}} = 0,$$

and, if $\ell = 0$, $\sum_{k=0}^{2n-1} \sin k\frac{\ell\pi}{n} = 0$. Note again, that $j \pm m$ is integer and its absolute value does not exceed $2n - 2$.

Combine (2.35), (2.36) and (2.37) to give

$$A_m = \frac{1}{n} \sum_{k=0}^{2n-1} \psi_k \cos m\frac{k\pi}{n} \qquad m = 1, \ldots, n-1.$$

- Show for B_m. If $m = n$ then $\sin(mk\pi/n) = 0$ and

$$B_n = 0 = \frac{1}{n} \sum_{k=1}^{2n-1} \psi_k \sin m\frac{k\pi}{n}$$

as required. Now consider $m = 1, \ldots, n-1$:

$$\frac{1}{n} \sum_{k=0}^{2n-1} \psi_k \sin m\frac{k\pi}{n} = \frac{1}{n} \sum_{k=0}^{2n-1} \left(A_0 \sin m\frac{k\pi}{n} + \sum_{j=1}^{n} A_j \cos j\frac{k\pi}{n} \sin m\frac{k\pi}{n} \right.$$

$$\left. + \sum_{j=1}^{n-1} B_j \sin j\frac{k\pi}{n} \sin m\frac{k\pi}{n} \right).$$

Now

$$\sum_{k=0}^{2n-1} A_0 \sin m\frac{k\pi}{n} = 0 \quad \text{(see above)};$$

$$\sum_{k=0}^{2n-1} \cos k\frac{j\pi}{n} \sin k\frac{m\pi}{n} = \frac{1}{2} \sum_{k=0}^{2n-1} \left(\sin k\frac{(j+m)\pi}{n} + \sin k\frac{(m-j)\pi}{n} \right) = 0;$$

$$\sum_{k=0}^{2n-1} \sin k\frac{j\pi}{n} \sin k\frac{m\pi}{n} = \frac{1}{2} \sum_{k=0}^{2n-1} \left(\cos k\frac{(j-m)\pi}{n} - \cos k\frac{(j+m)\pi}{n} \right)$$

$$= \begin{cases} 0, & j \neq m, \\ n, & j = m. \end{cases}$$

Hence we get

$$B_m = \frac{1}{n} \sum_{k=0}^{2n-1} \psi_k \sin m\frac{k\pi}{n} \qquad m = 1, \ldots, n-1,$$

as required.

- Show for A_n:

$$\frac{1}{2n} \sum_{k=0}^{2n-1} (-1)^k \psi_k = \sum_{k=0}^{2n-1} (-1)^k \left(A_0 + \sum_{j=1}^{n} A_j \cos j\frac{k\pi}{n} + \sum_{j=1}^{n-1} B_j \sin j\frac{k\pi}{n} \right).$$

Now $\sum\limits_{k=0}^{2n-1}(-1)^k A_0 = 0$ and (representing $(-1)^k = \cos k\frac{n}{n}\pi$)

$$\sum_{k=0}^{2n-1}\cos k\tfrac{n}{n}\pi \cos j\tfrac{k\pi}{n} = \tfrac{1}{2}\sum_{k=0}^{2n-1}\left(\cos k\tfrac{(n-j)\pi}{n} + \cos k\tfrac{(n+j)\pi}{n}\right)$$

$$= \begin{cases} 0, & \text{if } n \neq j\,, \\ \tfrac{1}{2}\cdot 4n = 2n, & \text{if } j = n\,, \end{cases}$$

$$\sum_{k=0}^{2n-1}\cos k\tfrac{n}{n}\sin j\tfrac{k\pi}{n} = \tfrac{1}{2}\sum_{k=0}^{2n-1}\left(\sin k\tfrac{(n-j)\pi}{n} + \sin k\tfrac{(n+j)\pi}{n}\right) = 0.$$

Hence

$$A_n = \tfrac{1}{2n}\sum_{k=0}^{2n-1}(-1)^k\psi_k$$

as required.

Similarly, it can be shown that function (2.34) with A_m and B_m defined by (2.23) satisfies

$$\Psi(k\pi/n) = \psi_k \qquad (k = 0, \ldots, 2n-1).$$

Evaluation of $\epsilon(\phi)$

If $\epsilon(\phi) \equiv \sum\limits_{m=1}^{n}(A_m \sin m\phi - B_m \cos m\phi)$ with A_m and B_m given by (2.23), then

$$\epsilon(\phi) = \tfrac{1}{n}\sum_{m=1}^{n-1}\left(\sin m\phi \sum_{k=0}^{2n-1}\psi_k \cos m\tfrac{k\pi}{n} - \cos m\phi \sum_{k=0}^{2n-1}\psi_k \sin m\tfrac{k\pi}{n}\right)$$

$$+ \tfrac{1}{2n}\sum_{k=0}^{2n-1}(-1)^k\psi_k \sin n\phi$$

$$= \tfrac{1}{n}\sum_{m=1}^{n-1}\sum_{k=0}^{2n-1}\psi_k \sin m\left(\phi - \tfrac{k\pi}{n}\right) + \tfrac{1}{2n}\sum_{k=0}^{2n-1}(-1)^k\psi_k \sin n\phi.$$

Interchanging the order of summation gives

$$\epsilon(\phi) = \frac{1}{n} \sum_{k=0}^{2n-1} \psi_k \sum_{m=1}^{n-1} \sin m \left(\phi - \frac{k\pi}{n} \right) + \frac{1}{2n} \sum_{k=0}^{2n-1} (-1)^k \psi_k \sin n\phi. \qquad (2.38)$$

Consider $\epsilon(\phi)$ at $\phi = k'\pi/n$ $(k' = 0, \ldots, 2n-1)$. Since $\sin(nk'\pi/n) = 0$, the last term in (2.38) is zero at these points. Introducing $K \equiv k - k'$ we rewrite (2.38) as

$$\epsilon(k'\pi/n) = \frac{1}{n} \sum_{k=0}^{2n-1} \psi_k \left(-\sum_{m=1}^{n-1} \sin m \frac{K\pi}{n} \right). \qquad (2.39)$$

Because

$$
\begin{aligned}
\sum_{m=1}^{n-1} \sin m \frac{K\pi}{n} &= \frac{\cos \frac{K\pi}{2n} - \cos\left((n-1/2)\frac{K\pi}{n} \right)}{2 \sin \frac{K\pi}{2n}} \\
&= \frac{\cos \frac{K\pi}{2n} - (-1)^K \cos \frac{K\pi}{2n}}{2 \sin \frac{K\pi}{2n}} \\
&= \sigma(K) \equiv
\begin{cases}
\cot \frac{K\pi}{2n}, & K \text{ odd,} \\[2mm]
0, & K \text{ even,}
\end{cases}
\end{aligned}
\qquad (2.40)
$$

formula (2.39) can be written as

$$\epsilon(\phi = k'\pi/n) = -\frac{1}{n} \sum_{k=0}^{2n-1} \psi_k \sigma(k - k'). \qquad (2.41)$$

2.4   Implementation in MATLAB

The key step is to determine $\{\theta_k\}$ by solving the non-linear system (2.25) with $\phi_j = j\pi/n$ and $\psi(\theta)$ assumed to be known. Formula (2.9) shows how $\psi(\theta)$ is determined in the case when the dependence $t = t(\theta)$ connecting the airfoil's boundary parameter with the polar angle in the $\bar{z}$ plane can be easily established. If the boundary of the airfoil is specified as a sequence of coordinates we define $\psi(\theta)$ using cubic interpolation.

We solve (2.25) using the iterative procedure:

$$\begin{cases} \theta_j^{[\ell+1]} = \phi_j + \dfrac{1}{n} \sum_{k=0}^{2n-1} \psi(\theta_k^{[\ell]})\sigma(k-j), \\ \theta_j^{[0]} = \phi_j \end{cases} \tag{2.42}$$

where, $j = 1, \ldots, 2n-1$ for each $\ell = 0, \ldots$.

Our numerical procedure requires an explicit form for the transformation $\tilde{z} = \tilde{z}(\zeta)$ defined by (2.5). This form is

$$\tilde{z} = \frac{1}{2}(\zeta + \sqrt{\zeta^2 - 4a^2}), \tag{2.43}$$

where the used branch of $\sqrt{\zeta^2 - 4a^2}$ satisfies the following conditions:

(a) $\sqrt{\zeta^2 - 4a^2} = \zeta + O(\zeta^{-1})$ as $|\zeta| \to \infty$;

(b) its Riemann surface is cut along a line which connects the branching points $\zeta = \pm 2a$ and lies entirely inside the airfoil.

Transformation (2.6) has a twofold purpose. Firstly, as we noted earlier, it enables us to center the origin of the new coordinate system on the image of the airfoil, which helps to achieve a better convergence of the iterative procedure. Secondly, this simple transformation can in some cases facilitate the choice of the coordinate system for which the θ-parametrization of the boundary in (2.8) becomes possible. If the image of the airfoil under (2.43) is not a star-shaped region, another mapping must be used instead of (2.6).

Mapping (2.5) applied to a slender airfoil may result in a shape with a protruding segment corresponding to the nose if the parameter a is taken from the permissible interval indiscriminately. This can worsen convergence or even make it impossible no matter what ε is chosen in (2.6). The same

difficulty arises when the airfoil is not properly oriented with respect to the axes of ζ. (Note however that the orientation of the airfoil with respect to the flow is given and so may not be altered.)

Convergence of the process (2.42) thus strongly depends on the choice of the characteristics: the value of a in (2.5), parameter ε and the orientation of the airfoil in the ζ-plane. Search for a suitable combination of these parameters can be carried out with a tool that uses them as an input and instantly provides a visual feedback by displaying the resulting image of the airfoil in the $\tilde{z}$-plane. We organise this search as follows.

Suppose that the chord of the airfoil is L. Let $\varepsilon_{\text{norm}}$ be a complex parameter. The mapping

$$\zeta_{\text{norm}} = \tilde{z}_{\text{norm}} + 1/\tilde{z}_{\text{norm}}$$

transforms the circle $\tilde{z}_{\text{norm}} = \varepsilon_{\text{norm}} + |1 - \varepsilon_{\text{norm}}|e^{it}$ ($t \in [0, 2\pi)$), into a Zhukovskii airfoil. We denote its chord by $l(\varepsilon_{\text{norm}})$. Now taking

$$a = a(\varepsilon_{\text{norm}}) = L/l(\varepsilon_{\text{norm}}), \quad \varepsilon = a\varepsilon_{\text{norm}}$$

and considering the image of the circle $\tilde{z} = \varepsilon + |a - \varepsilon|e^{i\theta}$ ($\theta \in [0, 2\pi)$) under the transformation (2.5) we obtain a Zhukovskii airfoil whose trailing edge is at $\zeta = 2a$ and whose chord is $al(\varepsilon_{\text{norm}}) = L$. Displaying this and the given airfoil in the same axes with their trailing edges juxtaposed at $\zeta = 2a(\varepsilon_{\text{norm}})$ we can observe the discrepancy between them and control it by changing $\varepsilon_{\text{norm}}$. The latter can be most conveniently done by making $\varepsilon_{\text{norm}}$ depend on the position of a movable object on the same screen (see Figure 2.3). The smaller the discrepancy between the noses of the airfoils is achieved the better becomes the chance that the image of the given airfoil under mapping (2.5) is an acceptable near-circle shape.
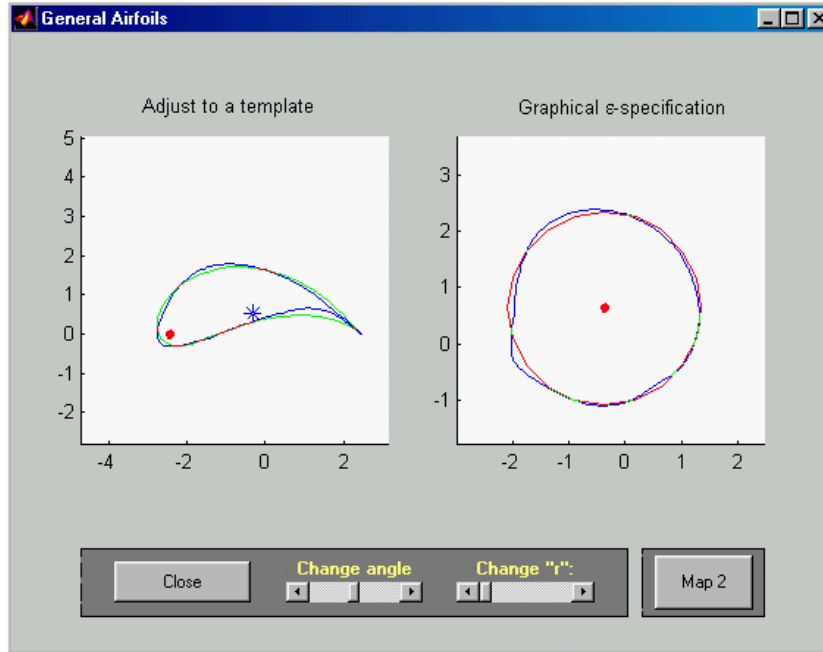

Anna Dostovalova, The University of Adelaide

Figure 2.3: Search for optimal mapping parameters using standard airfoils

A separate screen containing images of both airfoils in the $\tilde{z}$-plane provides an additional control over the described manipulations. Note that in such a procedure the required value for ε is obtained automatically.

When the system (2.25) has been solved we use (2.23) to define A_m and B_m. The transformation $\zeta(z)$ now can be written as

$$\zeta = \zeta(z) = \varepsilon + \bar{z}(z)e^{i\alpha_1} + \frac{a^2}{\varepsilon + \bar{z}(z)e^{i\alpha_1}} \ , \tag{2.44}$$

where

$$\bar{z}(z) = z \exp\left\{ \sum_{m=1}^{n}(A_m + iB_m)\left(\frac{z}{ae^{A_0}}\right)^{-m} \right\} \ .$$

The flow past the airfoil is given by formula (2.3) in which $\alpha_0 = \alpha - \alpha_1$ and Γ is defined by (2.30).

We have already noted that the method is applicable if the boundary of the near-circle admits parametrization in terms of the polar angle θ. It also essential that the function

$$\theta^\star(\phi) = \phi + \sum_{m=1}^{n} (B_m \cos m\phi - A_m \sin m\phi)$$

is one-to-one. This property does not simply follow from $\theta(\phi)$ being one-to-one but also depends on the behaviour of $\psi(\theta)$. If the near-circle has *salient* points, then $\theta^\star(\phi)$ is likely to be oscillatory in their neighbourhood no matter how large n is taken, a behavior akin to Gibbs' phenomenon.
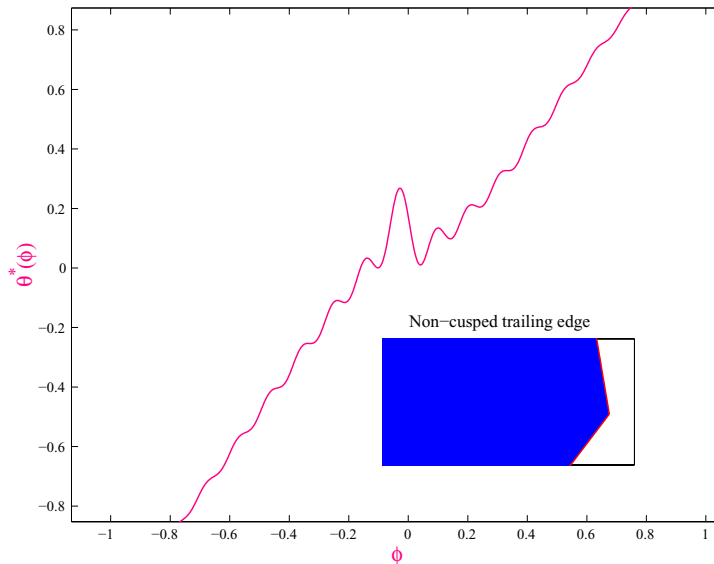
Figure 2.4: Typical behaviour of $\theta^*(\phi)$ for non-cusped geometry

Normally these considerations apply only to the point corresponding to the trailing edge of the airfoil. If mapping (2.5) is used, then, in order for the boundary of the near-circle to be smooth, the trailing edge must be

a cusp of the first kind. If the trailing edge represents a finite angle, the Zhukovskii transformation results in a near-circle with a corner point, which leads to oscillations of $\theta^\star(\phi)$, as shown on Figure 2.4 and self-intersections of the boundary of the approximating airfoil, on the computational level the procedure failing at the stage of solving equation (2.31) needed to satisfy the Kutta-Zhukovskii condition.

The Karman-Trefftz transformation is commonly used (as, for example in [10, 4]) instead of the Zhukovskii mapping to generate a near-circle without a corner point if the trailing edge angle is arbitrary.

2.5 Main states of the GUI

We implement the algorithm reviewed in Section 2.3 in the form of a single MATLAB m-function. In addition to the segment performing the iterative procedure (2.42), the tool incorporates interfaces for on-screen design of airfoils and choice of optimal mapping parameters needed for initial approximation. Post-processing options are provided including basic visualisation and storing data in a specific format.

Computer-aided airfoil shape generation uses second-order Bezier curves. Figure 2.5, representing the initial state of the GUI, shows such curves combined in an airfoil. Their control points are active and can be moved on the screen using the pointing device.

For the airfoil outline to remain smooth, the joint control points of the adjacent Bezier curves are only allowed to move along the segments between the respective middle control points, which as a result form vertices of a circumscribed polygon. The joint control points are shown as solid disks.

Anna Dostovalova, The University of Adelaide

Clicking on any of them with the right button refines the partition of the outline by adding to it a Bezier curve segment in the neighbourhood of the disk.
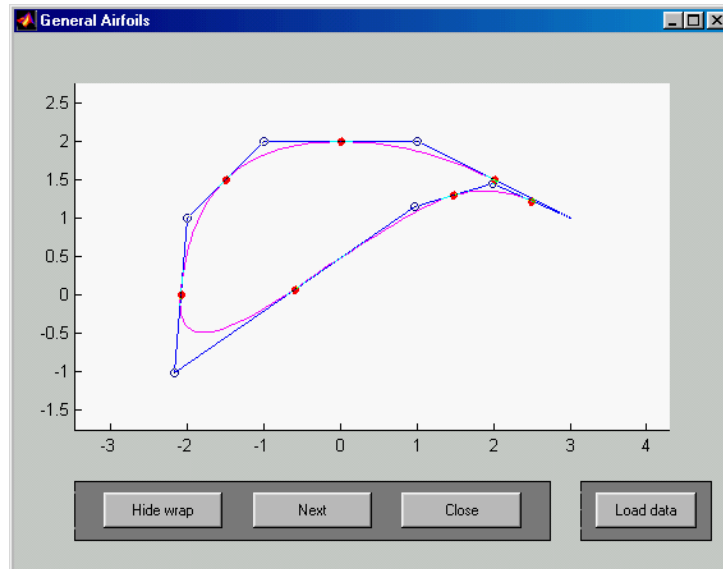

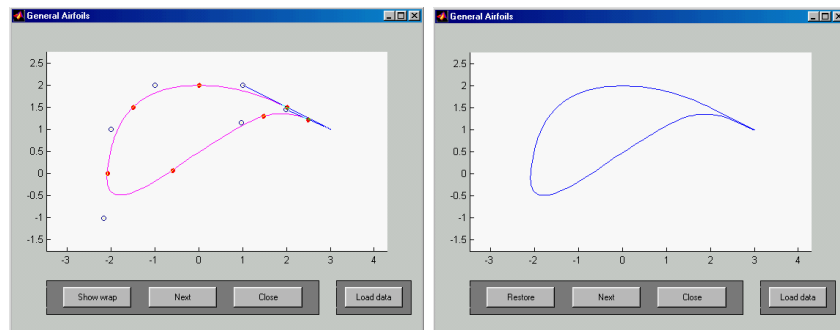Figure 2.5: On-screen shape generation

Figure 2.6: States of the shape generation mode

The sides of the polygon and the control points of the Bezier curves can be removed at any stage of the shape generation mode as shown in Figure 2.6.
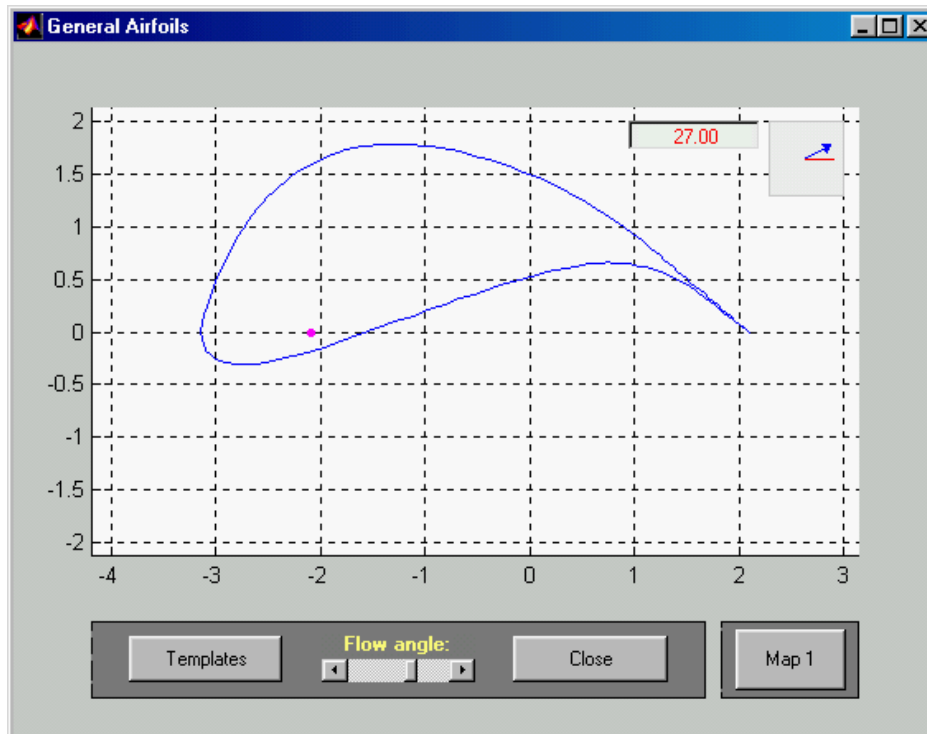

Figure 2.7: Default orientation of the airfoil

Figure 2.7 exhibits the state that occurs after the airfoil outline has been generated. The airfoil is oriented so that its longest chord is horizontal and it is this orientation with respect to which we shall measure the direction of the uniform flow.

The button "Load data" of the previous mode allows to access this state directly if the wing geometry is provided as an m-function `getwing`. Below we give an example of `getwing` for a non-symmetric Zhukovskii airfoil.

```
function Zeta=getwing
epsilon=-0.1+0.1i;
a=1;
N=100;
Z=epsilon+(a-epsilon)*exp(i*[0:N-1]*2*pi/N);
Zeta=Z+a^2./Z;
```
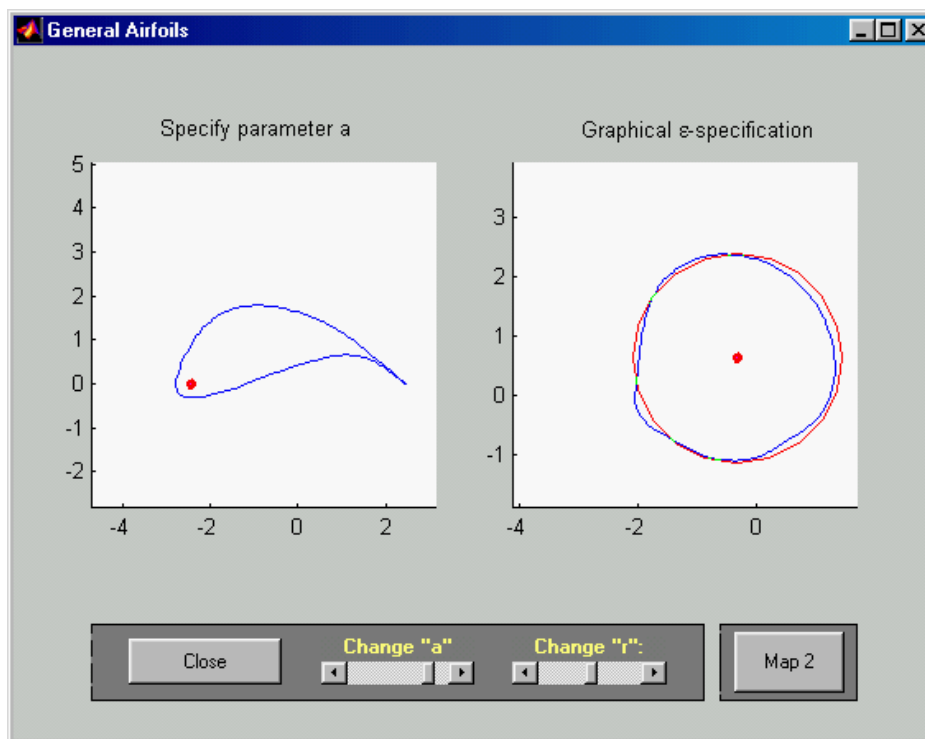

Figure 2.8: Determination of mapping parameters

Now we have to specify the mapping parameters a, ε and α_1. Buttons "Templates" and "Map 1" allow to proceed to one of the two possible states shown in Figures 2.3 and 2.8. The method of Figure 2.3 uses Zhukovskii's

airfoils and is described in Section 2.3. The state in Figure 2.8 uses a more straightforward but less effective method, in which the values of a and ϵ are decided on the basis of comparison of the image of the airfoil under the Zhukovskii mapping with circles. Pressing on the button "Map 2" brings the user to the control panel shown in Figure 2.9.

Figure 2.9: Setting up computation and post-processing parameters

Here one can set up such parameters as the number of iterations, or the number of points the approximating airfoil is to share with the exact airfoil. Visualisation and post-processing parameters can also be entered at this stage.

Pressing the button "Proceed" starts the iterative procedure whose aim is to determine $\{A_m, B_m\}$. When these coefficients have been found, the

program creates two standard figures as in Figure 2.10. One of them displays the original and the approximating airfoils to allow their comparison.
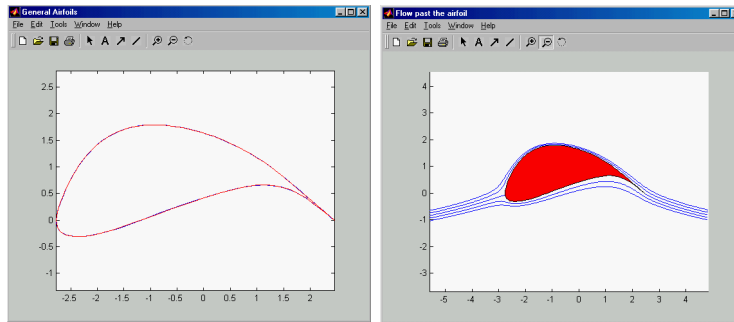

Figure 2.10: Basic visualisation

Another figure shows a few streamlines of the computed flow that pass near the airfoil. Visualisation provided within the tool is basic and was primarily intended to facilitate detection of possible errors in the code or calculations by examining local behaviour of the flow near the body, in particular near the stagnation point and the trailing edge.
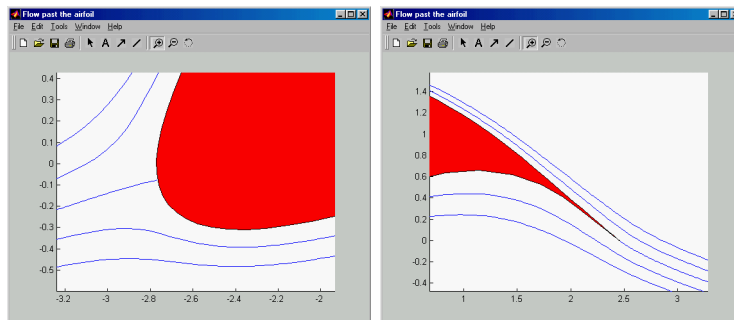

Figure 2.11: Flow near the stagnation point and the trailing edge

The obtained coefficients $\{A_m, B_m\}$ can be saved (using the pop-up menu "Save V-data?") in a mat-file for further interpretation, which could be some form of a 3D flow as shown in Figure 2.12 or various types of pressure-loading curves.
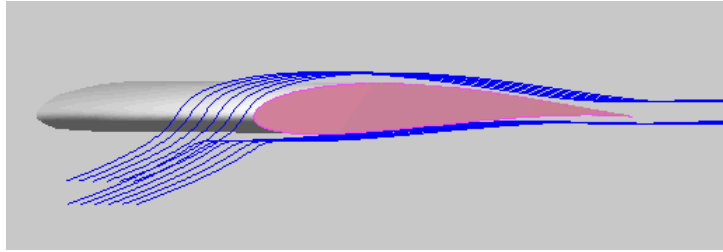

Figure 2.12: A variant of 3-D visualisation

Surface pressure distribution output can also be saved in the format described in 3.3 for subsequent boundary-layer computation.

2.6 Skin friction computation

Details of the numerical approach we use for evaluation of the skin friction and the required background are provided in Sections 1.2, 1.3 and 3.3.1, so we discuss here only the results of computation.

Behaviour of the boundary layer strongly depends on the shape of the obstacle and is very sensitive to its changes. The method of finite trigonometric series allows us to compute an exact inviscid flow past a shape approximating the original body, and we therefore have to examine how such an approximation affects parameters of the boundary layer, in particular the skin friction.

A readily available family of airfoils for which an exact inviscid solution can be obtained is the family of the Zhukovskii airfoils. The complex velocity

potential for flows past symmetric Zhukovskii airfoils is given by

$$f(\zeta) = U_\infty \left(z(\zeta) + \frac{R^2}{z(\zeta)} \right)$$

where $\zeta(z) = z + a^2/z$, $R = |a - \epsilon|$, $a > 0$ and $\epsilon < 0$. The parametric equation of the corresponding profile is

$$\zeta = (\epsilon + Re^t) + a^2/(\epsilon + Re^{it}), \quad t \in [0, 2\pi).$$

We can form the inviscid flow input using both the exact and approximate solutions, and compare the resulting skin friction curves. Figure 2.13 shows such curves for the following values of the parameters

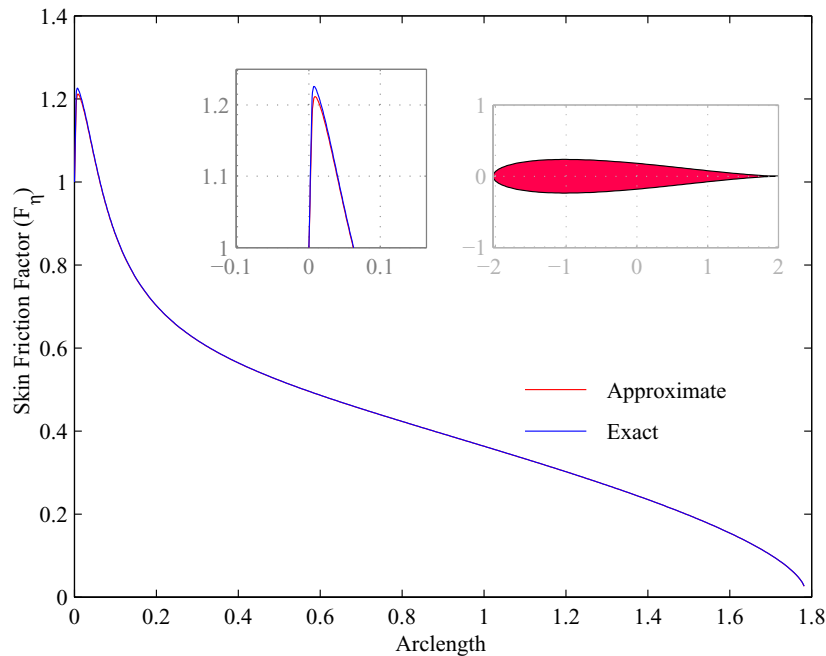$$a = 1, \quad \epsilon = -0.1, \quad n = 40, \quad N_{\text{iter}} = 150.$$

Figure 2.13: Approximate and exact skin friction plots for a Zhukovskii airfoil

The plots in Figure 2.13 are in a fairly good agreement. However, a straightforward application of the method of finite trigonometric series to thin airfoils does not give satisfactory results due to increasing influence of higher harmonics in the mapping $\Omega(z)$. For example, we were able to obtain the plot on Figure 2.14, showing the skin friction factor distribution for a Zhukovskii airfoil with $a = 1$ and $\epsilon = -0.034$, only using the exact solution.
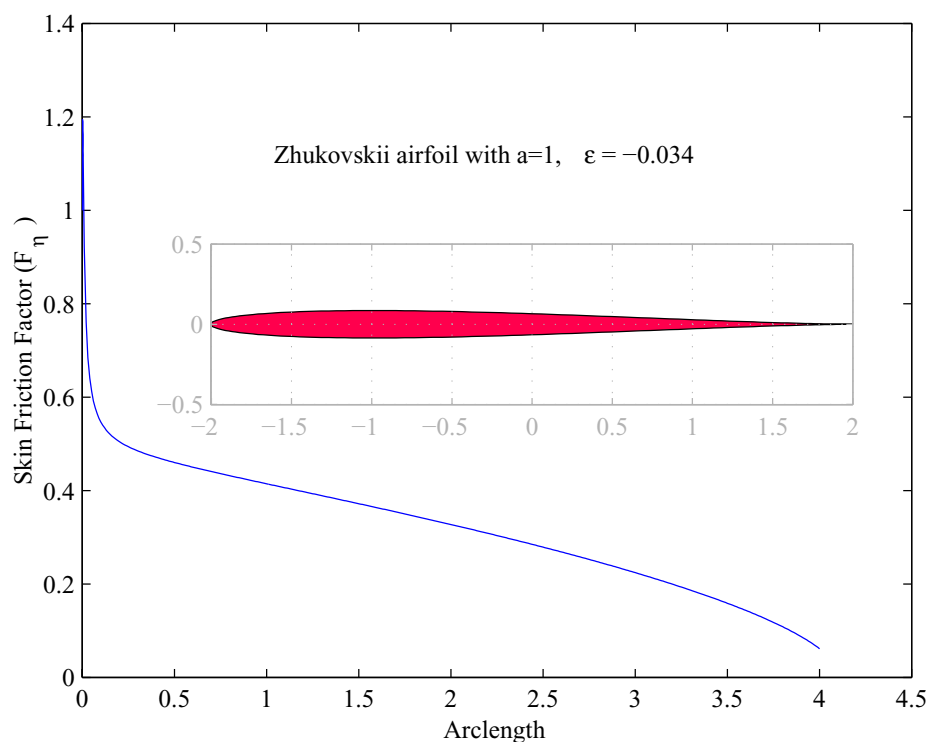

Figure 2.14: Skin friction factor for a Zhukovskii airfoil

Now consider a family of the airfoils whose upper/lower surfaces are given by

$$\zeta = x \pm i\mu(x), \qquad x \in [-F, B + T], \tag{2.45}$$

where F, B and T are positive and

$$\mu(x) = \begin{cases} H\left(1 - x^{2m}/F^{2m}\right)^{1/2}, & x \in [-F, 0) \\ H, & x \in [0, B) \\ \dfrac{H}{2}\left[1 - \text{th}\left(\tan\left(\dfrac{\pi}{T}(x - B - 0.5T)\right)\right)\right], & x \in [B, B + T] \end{cases}$$
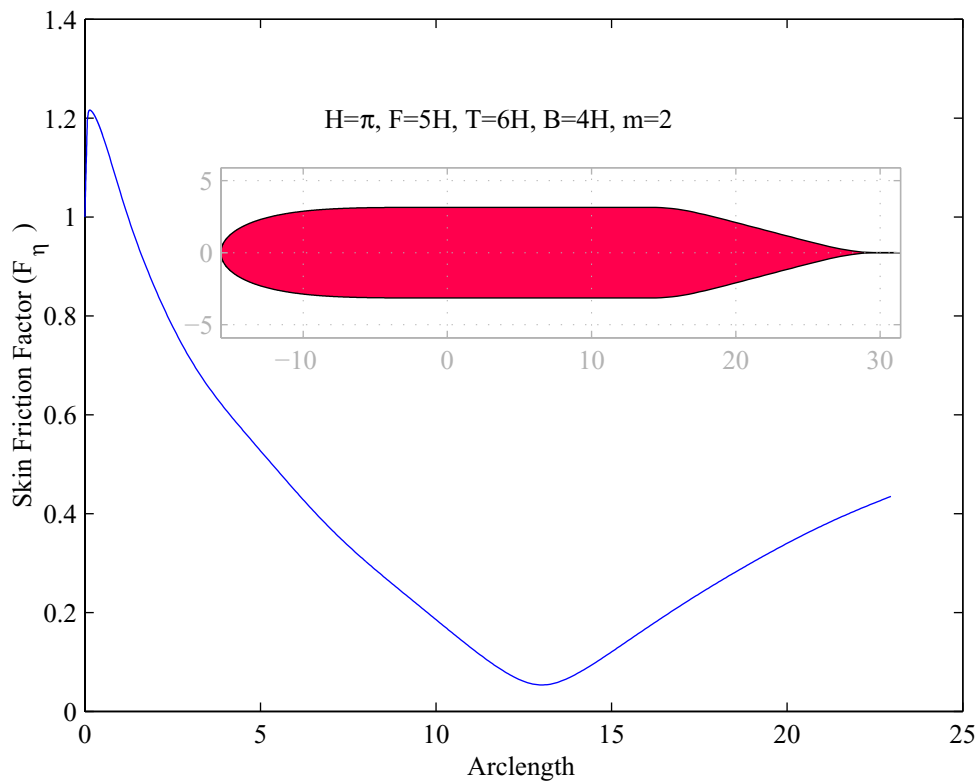

Figure 2.15: Skin friction factor for an airfoil described by (2.45)

Here we also assume that $m > 1$ which is a sufficient condition for the outline of the airfoil to be twice continuously differentiable at the point where its front face meets the body. The rear part of the airfoil (2.45) smoothly joins the body and the tail has a cusp.

Anna Dostovalova, The University of Adelaide

Figure 2.15 shows one of such airfoils and a computed skin friction factor.

In a practically interesting case of long airfoils, the ratios B/H and B/F are large and the flow behaviour near the nose of the body mainly depends on the geometry of the front face. Direct use of the Theodorsen–Naiman method for potential flow computation in this case yields an inviscid flow data resulting in an oscillatory skin-friction curve. We experienced a similar problem in the case of thin Zhukovskii airfoils. In order to deal with the problem when the airfoil is long, we replace it with a semi-infinite body which has the same front face, and develop a technique allowing us to overcome such difficulties. This is done in Chapter 3.

Chapter 3

Boundary layer computation for flows past long symmetric objects

3.1 Introduction

Symmetrical objects with very long straight bodies are often encountered in practice. Straightforward use of the Theodorsen–Naiman method as in Chapter 2 for computation of an inviscid component of the flow past such objects yields a solution with a noticeable presence of higher-order terms in the corresponding finite trigonometric series. Even though the resulting velocity potential can still be utilised for evaluation of the inviscid flow parameters, such as the pressure loading or the outer flow velocity magnitude, because of the oscillations induced by the higher-order harmonics, its use for the boundary layer computation becomes problematic.

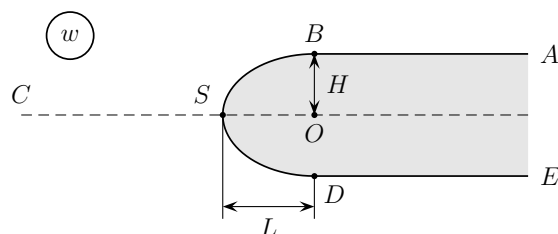If we assume that the body of the object is long enough so that the be-

Figure 3.1: Flow configuration in the physical plane.

haviour of the flow in the frontal region depends only on the shape of the front face and not on the body length, we can carry out the flow computation using the approximation by a semi-infinite obstacle. In this chapter we modify the technique for computation of flows past finite airfoils considered in Chapter 2 in order to apply it to the semi-infinite geometry. More specifically, we consider a symmetric semi-infinite obstacle with the front face of a generalised elliptic shape extending from $x = -L$ to $x = 0$, which smoothly joins a horizontal plate of constant width $2H$ at $x = 0$.

3.2   Inviscid solution

Consider a flow past a semi-infinite symmetrical body as shown in Figure 3.1.

In the following, the corresponding plane of a complex variable w is referred to as a physical plane, or simply as a w-plane. The speed of the flow at infinity is assumed to be $(U_\infty, 0)$.

3.2.1   Mapping to an auxiliary plane

First, we reduce a semi-infinite obstacle in a physical plane to an effectively finite body in an auxiliary ζ-plane by applying the Schwarz-Christoffel trans-

formation of the form

$$w(\zeta) = (\zeta - b)^{1/2}(\zeta + b)^{1/2} - 2b\log\left((\zeta - b)^{1/2} + (\zeta + b)^{1/2}\right)$$
$$+ b\log(2b) + b\pi i, \tag{3.1}$$

where $b = H/\pi$ and the branches of the square root and the logarithm have been chosen as follows:

$$V^{1/2} \equiv \sqrt{|V|}\exp\{i\arg(V)/2\}, \quad \arg(V) \in [0, 2\pi);$$
$$\log V \equiv \log|V| + i\arg(V), \quad \arg(V) \in [0, 2\pi).$$

The corresponding inverse transformation $\zeta(w)$ maps a half-plane $\operatorname{Im}\zeta > 0$ onto the part of the w-plane "above" the step $COBA$. The arc $S_\zeta B_\zeta$, the ζ-image of the arc SB of the front face, is sketched in Figure 3.2.
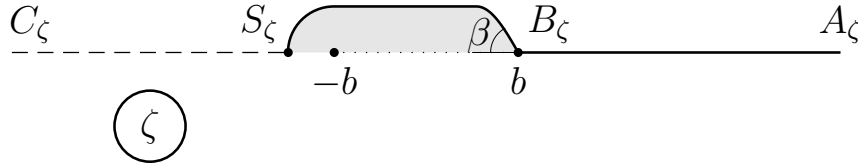
Figure 3.2: Image of the arc SB in the ζ-plane.

Since

$$w(-b) = 0 \text{ and } w(b) = ib\pi = iH,$$

the ζ-image of the point O is $\zeta = -b$, and B_ζ, the image of the point B, is at $\zeta = b$. The stagnation point S is mapped onto a point S_ζ at $\zeta = -s_0$, where s_0 is a positive number satisfying the equation

$$-L = -\sqrt{s_0^2 - b^2} - 2b\log\left(\sqrt{s_0 + b} + \sqrt{s_0 - b}\right) + b\log 2b. \tag{3.2}$$

Note. The shape of the arc $S_\zeta B_\zeta$ can be computed as follows. If the arc SB is specified in polar coordinates:

$$w(\theta) = R(\theta)e^{i\theta}, \quad \theta \in [\pi/2, \pi],$$

then, in order to obtain $r(t)$ for the parametrization of $S_\zeta B_\zeta$ in polar coordinates in the ζ-plane

$$\zeta(t) = r(t)e^{it}, \quad t \in [0, \pi],$$

we must solve the equation

$$\left|w(re^{it})\right| - R\left(\arg\left(w(re^{it})\right)\right) = 0$$

with respect to r for each required t.

Similarly, if the arc SB is specified in Cartesian coordinates, e.g. in the form $G(\operatorname{Re} w, \operatorname{Im} w) = 0$, then the equation for $r(t)$ is

$$G\left(\operatorname{Re} w(re^{it}), \operatorname{Im} w(re^{it})\right) = 0.$$

Since $w(\zeta)$ is analytic at $\zeta = -s_0 < -b$, the angle between the arc $S_\zeta B_\zeta$ and the segment $S_\zeta C_\zeta$ at S_ζ is the same as the angle between their prototypes in the w-plane.

In order to find β, or equivalently $\alpha = \pi - \beta$, the angles between $S_\zeta B_\zeta$ and $C_\zeta A_\zeta$ at B_ζ, we have to consider how $w(\zeta)$ behaves near $\zeta = b$.

First write

$$\frac{dw}{d\zeta} = \frac{(\zeta - b)^{1/2}}{(\zeta + b)^{1/2}}, \quad \text{or} \quad \frac{dw}{d\zeta} = g(\zeta)(\zeta - b)^{1/2}. \tag{3.3}$$

Note that $g(\zeta) = 1/(\zeta + b)^{1/2}$ is analytic in the neighbourhood of $\zeta = b$, so we can write

$$\frac{dw}{d\zeta} = \left(g(b) + c_1(\zeta - b) + \cdots + c_n(\zeta - b)^n + \cdots\right)(\zeta - b)^{1/2}$$

---

where $g(b) = 1/\sqrt{2b} \neq 0$. Hence

$$w(\zeta) = w(b) + \frac{2}{3}g(b)(\zeta - b)^{3/2} + O\left(|\zeta - b|^{5/2}\right),$$

or

$$w(\zeta) - w(b) = \frac{2}{3}g(b)(\zeta - b)^{3/2}\left(1 + O(|\zeta - b|)\right). \tag{3.4}$$

Representing a segment of $B_\zeta S_\zeta$ in the neighbourhood of B_ζ in the form

$$\zeta = \zeta(s) \equiv b + se^{i\alpha(s)} \quad (\alpha(s) \in (0, \pi))$$

we obtain from (3.4)

$$w(\zeta(t)) - w(b) = \frac{2}{3}g(b)s^{3/2}e^{i3\alpha(s)/2}(1 + O(s)).$$

Dividing by $s^{3/2}$ and letting s go to zero in the resulting expression we obtain:

$$\lim_{s \to 0} \frac{w(\zeta(s)) - w(b)}{s^{3/2}} = \frac{2}{3}g(b)e^{i3\alpha(0)/2}.$$

Since the left-hand side of this relation is negative and $g(b) > 0$, we have

$$\pi = \frac{3}{2}\alpha(0) \quad \Rightarrow \quad \pi - \beta \equiv \alpha = \alpha(0) = \frac{2}{3}\pi.$$

Thus $\beta = \pi/3$.

3.2.2 Formulation in the ζ-plane

Our aim is to construct a complex velocity potential $f(w)$ which describes a branching flow symmetrical with respect to the real axis of w and satisfies the condition at infinity

$$f'(w) \to U_\infty, \text{ as } |w| \to \infty.$$

Anna Dostovalova, The University of Adelaide

In order to avoid dealing with an arbitrary constant in the solution we will also require that $f(w) = 0$ at the stagnation point S. Hence $f(w)$ must satisfy the condition

$$\operatorname{Im} f(w) = 0, \tag{3.5}$$

on the boundary of the obstacle, since it coincides with the branching part of the stagnating streamline.

Consider $F(\zeta) \equiv f(w(\zeta))$ where $w(\zeta)$ is given by (3.1). From the conditions on $f(w)$ and (3.1) we derive the conditions allowing us to uniquely determine $F(\zeta)$.

Write $f(w) = \varphi(w) + i\psi(w)$ and denote the branching streamline by σ. By (3.5) we have: $\psi(w) = 0$, if $w \in \sigma$. If w belongs to the upper branch of σ, then its complex conjugate $\bar{w}$ belongs to its lower branch, so, by the reflection principle,

$$f(w) = \overline{f(\bar{w})} = f(\bar{w}). \tag{3.6}$$

Let us turn to the mapping $\zeta(w)$ now. If $w \in CS$, then $\operatorname{Im} \zeta(w) = 0$. Hence the analytic continuation of $\zeta(w)$ from the upper half-plane satisfies the reflection principle

$$\zeta(w) = \overline{\zeta(\bar{w})},$$

so it maps the front face BSD onto a symmetric wing-like profile. Since $\operatorname{Im} \zeta(w) = 0$, if $w \in BA$, we have

$$\zeta(w) = \zeta(\bar{w}), \quad w \in BA \cup DE. \tag{3.7}$$

This can also be seen directly from (3.1), as it shows that

$$w(\zeta + i0) = w(\zeta - i0) + 2Hi, \text{ if } \zeta \in [b, \infty).$$

Anna Dostovalova, The University of Adelaide

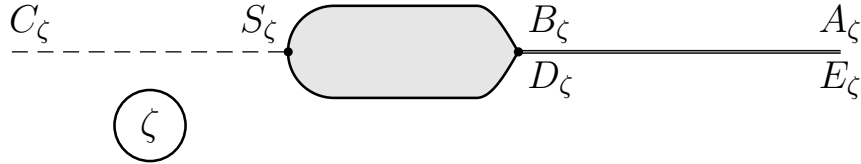Geometry of the obstacle in the ζ-plane is sketched in Figure 3.3.

Figure 3.3: Geometry of the obstacle in the ζ-plane

Combining (3.6) and (3.7) we find that

$$F(\zeta - i0) = F(\zeta + i0), \ \text{if } \zeta \in [b, \infty).$$

This means that $F(\zeta)$ is analytic in the exterior of the domain bounded by $B_\zeta S_\zeta D_\zeta$. Since $w/\zeta \to 1$ as $|\zeta| \to \infty$, the function $F(\zeta)$ can be expanded at sufficiently large $|\zeta|$ into a Laurent series of the form:

$$F(\zeta) = U_\infty \zeta + a_0 + \frac{a_1}{\zeta} + \frac{a_2}{\zeta^2} + \cdots . \tag{3.8}$$

We must also have $F(-s_0) = 0$ and

$$\text{Im } F(\zeta) = 0 \text{ if } \zeta \in C_\zeta S_\zeta \cup B_\zeta S_\zeta D_\zeta \cup B_\zeta A_\zeta . \tag{3.9}$$

Conditions (3.8) and (3.9) constitute a standard aerodynamic problem for a circulation-free flow past a symmetric airfoil $B_\zeta S_\zeta D_\zeta$. This problem is solved by constructing a conformal mapping $z(\zeta)$ which transforms $B_\zeta S_\zeta D_\zeta$ onto a circle $|z| = R$ and satisfies the condition

$$\zeta(z)/z \to 1, \ \text{as } |z| \to \infty .$$

The resulting $F(\zeta)$ has the form

$$F(\zeta) = \Phi(z(\zeta)), \text{ where } \Phi(z) = U_\infty(z + R^2/z)\,, \qquad (3.10)$$

and the flow in the physical plane is $f(w) = \Phi(z(\zeta(w)))$.

We can look at this result from a different point of view. Each finite symmetric wing $B_\zeta S_\zeta D_\zeta$ in the ζ-plane with the tail angle of $2\pi/3$ generates a flow past a semi-infinite body BSD in the w-plane. Below we consider conditions on such wing-like profiles which guarantee that the transition of the front face to the body in the w-plane is smooth. Non-smoothness of the body surface is one of the factors leading to separation of the boundary layer.

Take the upper boundary of the tail. We have already found that its parametrization

$$\zeta = b + se^{i\alpha(s)}$$

satisfies $\alpha(0) = 2\pi/3$. We will assume that $\alpha(s)$ is a smooth function.

Suppose that

$$\zeta = b + se^{i\alpha_0(s)} \equiv \zeta_0(s)$$

is the image of the line $w = iH - t$, $t > 0$, under the mapping $\zeta = \zeta(w)$. Introduce

$$\delta(s) \equiv \alpha(s) - \alpha_0(s).$$

The front face can be described in the complex plane of $w = x_w + iy_w$ by the parametric equations

$$x_w = \operatorname{Re} w(\zeta(s)), \qquad (3.11)$$

$$y_w = \operatorname{Im} w(\zeta(s)). \qquad (3.12)$$

Eliminating s, we reduce these parametric equations to the form $y_w = y_w(x_w)$.

The following result is valid:

If $\delta(s) = O(s^\gamma)$, as $s \to 0$, and $\gamma > 0$, then $y_w(x_w) - H = O(x_w^{2\gamma/3+1})$.

$$(3.13)$$

Let us prove this result. We have shown above that

$$w(\zeta) = iH + G(\zeta)(\zeta - b)^{3/2}$$

where $G(\zeta)$ is analytic in the neighbourhood of $\zeta = b$, and

$$G(b) = \frac{2}{3}\frac{1}{\sqrt{2b}} \neq 0.$$

Hence (3.11) can be written as

$$
\begin{aligned}
x_w(s) &= \mathrm{Re}\left\{G(\zeta(s))s^{3/2}e^{i\frac{2}{3}\alpha(s)}\right\} \\
&= \mathrm{Re}\left\{(G(b) + O(s))\,s^{3/2}\left(e^{i\pi} + O(s^\gamma)\right)\right\} \\
&= \left(-G(b) + O\left(s^{\min(1,\gamma)}\right)\right)s^{3/2}.
\end{aligned}
$$

$$(3.14)$$

Similarly,

$$
\begin{aligned}
y_w - H &= \mathrm{Im}\left\{G(\zeta(s))s^{3/2}e^{i\frac{2}{3}\alpha(s)}\right\} \\
&= \mathrm{Im}\left\{G\left(\zeta_0(s) + O(s^{\gamma+1})\right)s^{3/2}\left(e^{i\frac{2}{3}\alpha_0(s)} + O(s^\gamma)\right)\right\} \\
&= O\left(s^{\gamma+3/2}\right),
\end{aligned}
$$

$$(3.15)$$

since

$$\mathrm{Im}\left\{G(\zeta_0(s))s^{3/2}e^{i\frac{2}{3}\alpha_0(s)}\right\} = \mathrm{Im}\{w(\zeta_0(s)) - iH\} = 0.$$

Combining (3.14) and (3.15) we obtain that

$$\left|\frac{y_w(x_w) - H}{x_w^{\frac{2}{3}\gamma+1}}\right| = \left|\frac{O(s^{\gamma+3/2})}{\left(-G(b) + O\left(s^{\min(1,\gamma)}\right)\right)^{\frac{2}{3}\gamma+1}s^{\gamma+3/2}}\right| \leq C$$

for some positive C and small s, which is the required result.

Note. We can easily derive from this result a sufficient condition for continuity of the derivatives of $y_w(x_w)$ at $x_w = 0$. If $\gamma > \frac{3}{2}(N-1)$, then

$$\left. \frac{d^k y_w}{dx_w^k} \right|_{x_w = 0-0} = 0 \quad (k = 1, \dots, N),$$

and the function $y_w(x_w)$ is continuously differentiable N times at $x_w = 0$.

Formula (3.10) suggests that in the Laurent series for $F(\zeta)$ the coefficients a_0 and a_1 satisfy

$$a_0 = \lim_{|\zeta| \to \infty} (z(\zeta) - \zeta) \quad \text{and} \quad a_1 = R^2.$$

Furthermore, by (3.9), $\text{Im}\, a_0 = 0$.

Given $z(\zeta)$, let us determine, up to the terms of order $O(w^{-1})$, the asymptotic behaviour of the complex velocity potential at large w. As $|\zeta| \to \infty$, we have

$$w(\zeta) = \zeta - b \log \zeta + b \log(b/2) + b\pi i + O(\zeta^{-1}). \tag{3.16}$$

Hence

$$w = \zeta(1 + \mu_0(\zeta)), \text{ where } \mu_0 \to 0 \text{ as } |\zeta| \to \infty,$$

and so

$$\zeta = w(1 + \eta_0(w)), \text{ where } \eta_0 \to 0 \text{ as } |w| \to \infty.$$

This formula and (3.16) give

$$\zeta = w + b \log w - b \log(b/2) - b\pi i + \eta_1(w),$$

where $\eta_1 \to 0$ as $|w| \to \infty$. Repeated substitution into (3.11) gives an estimate for $\eta_1(w)$

$$\eta_1(w) = b^2 w^{-1} \log w + O(|w|^{-1}).$$

Anna Dostovalova, The University of Adelaide

Therefore

$$
\begin{aligned}
f(w) \equiv & F(\zeta(w)) = \zeta(w) + a_0 + O(|w|^{-1}) \\
= & w + b\log w - b\log(b/2) - b\pi i + b^2 w^{-1}\log w + a_0 + O(|w|^{-1}) \\
= & w + \frac{H}{\pi}\log w - \frac{H}{\pi}\log\frac{H}{2\pi} - Hi + \frac{H^2}{\pi^2 w}\log w + a_0 + O(|w|^{-1}).
\end{aligned}
$$

Note that, if $w = -s$, or $w = \pm iH + s$, and $s \to +\infty$, then, as expected, the principal part of this formula is real. The combination of terms on the right which do not vanish at infinity describe a flow past a body known as a semi-infinite Rankine ovoid. This profile will be used for testing purposes.

3.2.3   Mapping to the circle plane

We construct the mapping $z(\zeta)$, which conformally transforms the profile $B_\zeta S_\zeta D_\zeta$ onto a circle, using the following steps

$$\zeta \leftrightarrow \tilde{z} \leftrightarrow \bar{z} \leftrightarrow z.$$

Karman-Trefftz transformation

The mapping $\zeta \leftrightarrow \tilde{z}$ is the Karman-Trefftz transformation defined by

$$\left(\frac{\zeta - \zeta_0}{\zeta - \zeta_1}\right) = \left(\frac{\tilde{z} - \nu\zeta_0}{\tilde{z} - \nu\zeta_1}\right)^{1/\nu} \tag{3.17}$$

where $\nu = \pi/(2\pi - 2\beta)$, $\zeta_0 = b$ and ζ_1 is some point on the real axis inside domain bounded by $B_\zeta S_\zeta D_\zeta$ as shown in Figure 3.4.

Explicit forms of $\tilde{z}(\zeta)$ and $\zeta(\tilde{z})$ can be derived from (3.17)

$$\tilde{z} = \nu\frac{\zeta_0 - \zeta_1 S(\zeta; \zeta_0, \zeta_1)}{1 - S(\zeta; \zeta_0, \zeta_1)}, \tag{3.18}$$

$$\zeta = \frac{\zeta_0 - \zeta_1 K(\tilde{z}; \zeta_0, \zeta_1)}{1 - K(\tilde{z}; \zeta_0, \zeta_1)}, \tag{3.19}$$

where

$$S(\zeta; \zeta_0, \zeta_1) = \left(\frac{\zeta - \zeta_0}{\zeta - \zeta_1}\right)^{\nu} \quad \text{and} \quad K(\tilde{z}; \zeta_0, \zeta_1) = \left(\frac{\tilde{z} - \nu\zeta_0}{\tilde{z} - \nu\zeta_1}\right)^{1/\nu}.$$
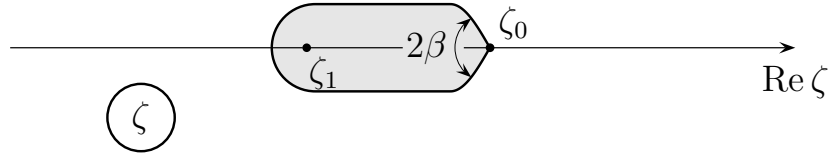

Figure 3.4: Parameters of the Karman–Trefftz transformation

The Karman-Trefftz transformation is used because of its "corner elimi-nation" property: it transforms the wing-like profile sketched in Figure 3.4 into a rounded shape, which we will call following [1] a *near-circle.*

The fact that the corner is mapped onto a smooth segment can be verified by using (3.17) and representing $\tilde{z}(\zeta)$ near ζ_0 as

$$\tilde{z} = \tilde{z}(\zeta_0) + \sigma(\zeta)(\zeta - \zeta_0)^{\nu}, \tag{3.20}$$

where $\sigma(\zeta)$ is analytic in the neighbourhood of ζ_0 and $\sigma(\zeta_0) = \nu(\zeta_0 - \zeta_1)^{1-\nu}$. If ζ is on the upper (lower) arc of the profile near the corner point ζ_0, s is the distance from ζ to ζ_0 and $\alpha_1(s)$ $(\alpha_2(s))$ is the angle between $\zeta - \zeta_0$ and the real axis, then

$$\zeta - \zeta_0 = se^{i\alpha_1(s)} \qquad \left(\zeta - \zeta_0 = se^{i\alpha_2(s)}\right),$$

and (3.20) gives

$$\tilde{z} - \tilde{z}(\zeta_0) = \sigma(\zeta_0)s^{\nu}e^{i\nu\alpha_1(0)} + O(s^{\nu+1}) \qquad \text{for the upper arc,}$$

$$\tilde{z} - \tilde{z}(\zeta_0) = \sigma(\zeta_0)s^{\nu}e^{i\nu\alpha_2(0)} + O(s^{\nu+1}) \qquad \text{for the lower arc.}$$

Hence

$$\lim_{s \to 0+} \frac{\tilde{z} - \tilde{z}(\zeta_0)}{s^\nu} = \sigma(\zeta_0) e^{i\nu\alpha_1(0)}, \quad \text{(upper arc)},$$

$$\lim_{s \to 0+} \frac{\tilde{z} - \tilde{z}(\zeta_0)}{s^\nu} = \sigma(\zeta_0) e^{i\nu\alpha_2(0)}, \quad \text{(lower arc)}.$$

We can see now, that because

$$\nu\alpha_1(0) - \nu\alpha_2(0) = \nu(2\pi - 2\beta) = \frac{\pi(2\pi - 2\beta)}{(2\pi - 2\beta)} = \pi,$$

the $\tilde{z}$-image of the profile $B_\zeta S_\zeta D_\zeta$ near $\tilde{z}(\zeta_0)$ is smooth.

Formula (3.20) also shows that $\lim_{|\zeta| \to \infty} \tilde{z}(\zeta)/\zeta = 1$. To verify this note that, as $|\zeta| \to \infty$,

$$S(\zeta) = 1 - \nu(\zeta_0 - \zeta_1)\zeta^{-1} + O(|\zeta|^{-2}),$$

which gives

$$\tilde{z} = \frac{\nu(\zeta_0 - \zeta_1 + O(|\zeta|^{-1}))}{\nu(\zeta_0 - \zeta_1)\zeta^{-1} + O(|\zeta|^{-2})} = \zeta(1 + O(|\zeta|^{-1})).$$

In our numerical procedure we will use the formula

$$\frac{d\zeta}{d\tilde{z}} = \frac{(\zeta_0 - \zeta_1)^2 K(\tilde{z}; \zeta_0, \zeta_1)}{(1 - K(\tilde{z}; \zeta_0, \zeta_1))^2 (\tilde{z} - \nu\zeta_0)(\tilde{z} - \nu\zeta_1)}, \tag{3.21}$$

which can be obtained from (3.19) by straightforward differentiation. Since $K \sim (\tilde{z} - \nu\zeta_0)^{1/\nu}$ and $1/\nu > 1$, this formula shows that $\lim_{\tilde{z} \to \nu\zeta_0} \zeta'(\tilde{z}) = 0$.

Mapping from the near-circle plane

The image of the stagnation point S in the $\tilde{z}$ plane is a point $\tilde{z}_S$ on the real axis:

$$\tilde{z} = \tilde{z}(\zeta = -s_0),$$

where s_0 and $\tilde{z}(\zeta)$ are defined by (3.2) and (3.18). Introducing a parameter a as

$$a = 0.5(\nu b - \tilde{z}_S)$$

we define the mapping $\tilde{z} \leftrightarrow \bar{z}$ as a simple shift along the real axis

$$\bar{z} = \tilde{z} - \tilde{z}_S - a, \tag{3.22}$$

needed to center the contour at the origin.

The boundary of the near-circle can be parametrized as $\bar{z} = ae^{\psi(t)+it}$.

Introduce

$$\Omega(z) = \sum_{m=1}^{n} (A_m + iB_m) \left(ae^{A_0}/z\right)^m \tag{3.23}$$

where

$$
\begin{aligned}
A_0 &= \frac{1}{2n} \sum_{k=0}^{2n-1} \psi_k \, , \\
A_m &= \frac{1}{(1+\delta_{mn})n} \sum_{k=0}^{2n-1} \psi_k \cos m\frac{k\pi}{n} \qquad (m = 1, \ldots, n)\,, \\
B_m &= \frac{1}{n} \sum_{k=0}^{2n-1} \psi_k \sin m\frac{k\pi}{n} \qquad (m = 1, \ldots, n)\,, \\
\psi_k &= \psi(t_k)
\end{aligned}
\tag{3.24}
$$

and t_k are solutions of the nonlinear system:

$$t_k - k\pi/n = \frac{1}{n} \sum_{m=0}^{2n-1} \psi(t_m)\sigma(m-k), \qquad k = 0, \ldots, 2n-1\,, \tag{3.25}$$

$$\sigma(K) \equiv \begin{cases} \cot(K\pi/2n), & K \text{ odd} \\ 0, & K \text{ even.} \end{cases}$$

Anna Dostovalova, The University of Adelaide

The mapping $\bar{z} = ze^{\Omega(z)}$ transforms the set $|z| \geq ae^{A_0}$ onto the exterior of the domain bounded by the contour

$$\bar{z} = ae^{\psi^\star(t)+it}$$

where $\psi^\star(t)$ has the property

$$\psi^\star(t_k) = \psi(t_k) \qquad (k = 0, \ldots, 2n - 1).$$

Hence the transformation $w = w(\zeta(z))$ maps the circle $|z| = ae^{A_0}$ onto a contour which shares with the original front face at least $2n$ common points. The resulting solution describes an exact flow past such an approximate profile.

Note. The algorithm that carries out the transformations described here and computes the inviscid flow has been implemented in MATLAB [18]. If the coefficients A_m and B_m $(m = 1, \ldots, n)$ are arranged in row-vectors

$$A = [A_1, \ldots, A_n],$$
$$B = [B_1, \ldots, B_n],$$

then the points z_k stored as components of the complex row-vector

$$z = [z_1, \ldots, z_N]$$

are mapped under the transformation

$$\bar{z}(z) = ze^{\sum\limits_{m=1}^{n}(A_m+iB_m)(R/z)^m} \tag{3.26}$$

into points $[\bar{z}_1, \ldots, \bar{z}_N]$. The corresponding complex row-vector can be evaluated using MATLAB as

```
zB=z.*exp((A+i*B)*(ones(n,1)*(Rz./z)).^([1:n]'*ones(1,N)));
```

($\texttt{zB} \sim [\bar{z}_1, \ldots, \bar{z}_N]$).

The values of the derivative

$$\bar{z}\,'(z) = \left(1 - \sum_{m=1}^{n} m(A_m + iB_m)(R/z)^m\right)\bar{z}/z \qquad (3.27)$$

at z_k are found using

```
dzBdz=1-((A+i*B).*[1:n])*(ones(n,1)*(Rz./z)).^([1:n]'*ones(1,N));
dzBdz=dzBdz.*zB./z;
```

where

$$\texttt{dzBdz} \sim [\bar{z}\,'(z_1), \ldots, \bar{z}\,'(z_N)] \quad \text{and} \quad \texttt{zB} \sim [\bar{z}_1, \ldots, \bar{z}_N].$$

The inviscid flow solution provides us with the outer velocity which we will use in the boundary layer computation. The complex velocity potential of the outer flow is

$$f(w) = \Phi(z(\underbrace{\tilde{z}(\zeta(w)) - \tilde{z}_S - a}_{\bar{z}}))$$

and the complex velocity is

$$f'(w) = \Phi'(z)z'(\bar{z})\tilde{z}\,'(\zeta)\zeta'(w) = \Phi'(z)\frac{1}{\bar{z}\,'(z)}\frac{1}{\zeta'(\tilde{z})}\frac{1}{w'(\zeta)} \,. \qquad (3.28)$$

Since we have analytic expressions for $\bar{z}\,'(z)$ (formula (3.27)), $\zeta'(\tilde{z})$ (formula (3.21)), $w'(\zeta)$ (formula (3.3)), $w(\zeta)$ (formula (3.1)), $\zeta(\tilde{z})$ (formula (3.19)), $\tilde{z}(\bar{z})$ (formula (3.22)) and $\bar{z}(z)$ (formula (3.26)), computation of w and $f'(w)$ for a given z is straightforward.

The inviscid flow computation can now be summarised as follows:

1. Specify the front face in the physical plane.

2. Find the image of the front face in the ζ plane.

3. Map to the $\tilde{z}$ and then to the $\bar{z}$ planes (a is obtained at this stage).

4. Find A_0 and $\{A_m, B_m\}$ used in the mapping $\bar{z} = ze^{\Omega(z)}$;

5. The approximating front face in the physical plane is the image of

$$z = ae^{A_0 + i\phi}, \qquad \phi \in [0, 2\pi)$$

under the mapping $z \to \bar{z} \to \tilde{z} \to w$. Find the inviscid flow past the semi-infinite body with this approximate front face. Because of the symmetry, the images of the stagnation and the rearmost points of the front face of the approximate profile coincide at each mapping stage with the images of the stagnation and the rearmost points of the original shape.

6. Generate data for the boundary layer computation.

3.3 Boundary Layer Computation

3.3.1 Summary of the method

Here we provide only a summary of the numerical method we use for the boundary layer computation. Details and derivations can be found in Sections 1.2 and 1.3.

Steady two-dimensional laminar flow of a viscous fluid near a curved surface is governed by Prandtl's boundary layer equations (1.3)–(1.4) which can be written in the non-dimensional form as

$$\frac{\partial u}{\partial s} + \frac{\partial v}{\partial n} = 0 \ , \tag{3.29}$$

$$u\frac{\partial u}{\partial s} + v\frac{\partial u}{\partial n} = u_e(s)\frac{du_e}{ds} + \frac{\partial^2 u}{\partial n^2} \ , \tag{3.30}$$

where $u_e(s) = U_e(sL_c)/U_\infty$, L_c is a characteristic length. With the introduction of the Görtler variables (ξ, η) and (F, V) defined as

$$\xi = \int_0^s u_e(s)ds, \quad \eta = \frac{u_e}{\sqrt{2\xi}}n ,$$

$$u = Fu_e, \quad v = \frac{u_e}{2\xi}V - \frac{\partial\eta}{\partial s}\sqrt{2\xi}F ,$$

this system is transformed into

$$2\xi F_\xi + F + V_\eta = 0 ,$$
$$2\xi F F_\xi + V F_\eta + \sigma^p(\xi)(F^2 - 1) = F_{\eta\eta} , \tag{3.31}$$

where $\sigma^p(\xi) = 2\xi u_e'(s(\xi))/u_e^2(s(\xi))$.

Equations (3.31) must be solved subject to the boundary conditions

$$F(\xi, 0) = V(\xi, 0) = 0 \quad \text{and} \quad \lim_{\eta\to\infty} F(\xi, \eta) = 1 . \tag{3.32}$$

The numerical procedure used for solution of (3.31)–(3.32) is described in Section 1.3.

We organized the corresponding solver in a separate program, which will be referred to as a BLC-module. This module uses the arclength from the stagnation point $\bar{s}$ and the inviscid flow data ξ and σ^p as an input, its output consists of the values of the skin friction factor

$$\tau = \left.\frac{\partial F}{\partial\eta}\right|_{\eta=0}$$

and the corresponding values of the arc-length $\bar{s}$.

We take a fine mesh of points covering a segment of the front face between the stagnation point and some point on its upper part, and generate

sequences of values for

$\bar{s}$, the arclength measured from the stagnation point,

$$\xi(\bar{s}) = \int_0^{\bar{s}} U_e(\bar{s})d\bar{s}/(U_\infty L) \ ,$$

$$\sigma^p(\bar{s}) = \frac{2LU_\infty}{U_e^2(\bar{s})} \, \xi \, U_e'(\bar{s}) \ .$$

needed for the boundary layer computation. The BLC-module employs the same numerical technique as the program described in Chapter 1 written specifically for near-parabolic shapes. The module has been built to be used for computation of flows past generally shaped bodies as all required information about the geometry of the obstacle is now contained in the input data (3.33). Testing of the BLC module on a flow past a parabola gives the same plots for the skin-friction factor as in [36].
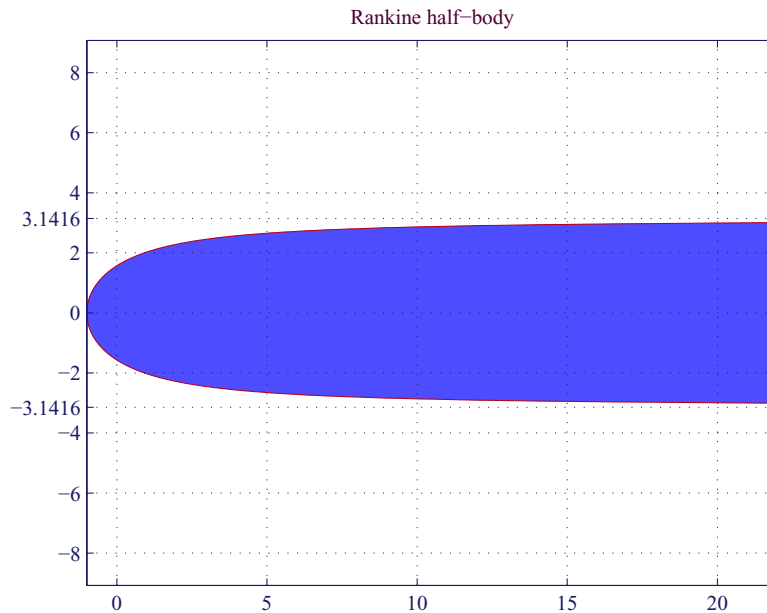

Figure 3.5: Limiting form of Rankine's ovoid

Anna Dostovalova, The University of Adelaide

A classical example of a semi-infinite body for which an inviscid solution can be obtained explicitly is a limiting form of Rankine's ovoid shown in Figure 3.5. The parametric equation of its boundary is

$$|w(\theta)| = \frac{H}{\pi} \frac{(\pi - \theta)}{\sin \theta}, \qquad \theta \in (0, 2\pi),$$

and the corresponding complex velocity potential is given by

$$f(w) = w + \frac{H}{\pi} \log w - iH$$

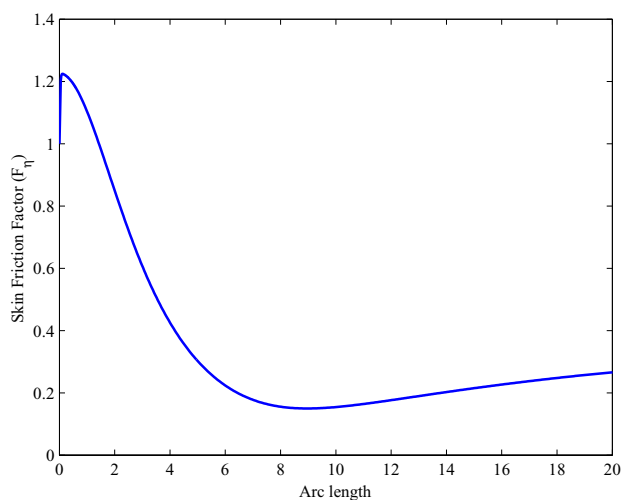where, as before, $\log w \equiv \log |w| + i \arg(w)$, and $\arg(w) \in [0, 2\pi)$.

Figure 3.6: Skin friction factor for the Rankine semi-infinite body

The plot of the skin friction factor obtained for the Rankine semi-infinite body is given in Figure 3.6. We can see from this plot that the skin friction

factor $\tau(\bar{s})$ is always positive, and so boundary layer separation does not occur.

If $f(w)$ cannot be obtained in explicit form, it is more convenient to form the mesh in the z-plane first:

$$z_m^{[k]} = ae^{A_0 + i\phi_m^{[k]}},$$

where $k = 0, \ldots, M - 1$, M is sufficiently large, $m = 1, 2$, and

$$\phi_m^{[k]} = \begin{cases} \pi - k\pi/M, & \text{if } m = 1 \,, \\ \pi - (k + 0.5)\pi/M, & \text{if } m = 2 \,. \end{cases}$$

The derivatives $w'(z)$ and $f'(w)$ are evaluated at $z_m^{[k]}$ using (3.3), (3.21), (3.27) and (3.28). These values are used to find (3.33) at $z_m^{[k]}$ numerically. Cubic interpolation is used to obtain σ^p at arbitrary ξ.

Formally σ^p is not defined at the stagnation point where $U_e = 0$, so we set σ^p at $\bar{s} = 0$ to

$$\sigma^p(0+) \equiv \lim_{\bar{s} \to 0+} \sigma^p(\bar{s}) = 1. \tag{3.33}$$

In order to verify (3.33) first assume that, as $\bar{s} \to 0$ we have

$$U_e(\bar{s}) = \kappa \bar{s}^\lambda + o(\bar{s}^\lambda) \qquad (\lambda > 0) \,,$$

and also

$$U_e'(\bar{s}) = \frac{\lambda \kappa}{\bar{s}}(\bar{s}^\lambda + o(\bar{s}^\lambda)) \,,$$

$$\int_0^{\bar{s}} U_e(\bar{s})d\bar{s} = \frac{\kappa \bar{s}^{\lambda+1}}{\lambda + 1} + o(\bar{s}^{\lambda+1}) \,.$$

Substitute this into (3.33) to obtain

$$\lim_{\bar{s} \to 0} \sigma^p(\bar{s}) = \frac{2\lambda}{\lambda + 1} \,.$$

To show that in our case $\lambda = 1$ note that

$$\frac{d}{dz}f(w(z))\Big|_{z=-R+\Delta z} = U_\infty\left(1 - \frac{R^2}{(-R+\Delta z)^2}\right) \simeq -\frac{2U_\infty}{R}\Delta z\,.$$

Therefore, since $w'(z) \neq 0$ at $z = -R$, we obtain

$$U_e(\bar{s}) = \left|\frac{d}{dw}f\left(w(-R+\Delta z)\right)\right| \simeq \frac{2U_\infty}{R|w'(-R)|^2}\bar{s}\,,$$

as required.

3.3.2   Application remarks and results

The front face of a semi-infinite body can be characterized by the aspect ratio L/H. We have seen that the Rankine half-body, whose aspect ratio is infinity, yields an unseparated flow. In reality we have to deal with bodies whose front face has a finite aspect ratio. Minimising L/H while keeping the flow unseparated is a task of practical interest. We will pursue this task by considering a particular family of front faces in a horizontal flow having unit speed at infinity.

The following observation will allow us to generalise our results to the case of non-unit flow speeds and scaled copies of the obstacle.

Consider an inviscid flow past a body B. Suppose that at infinity the flow is uniform and its speed is $(U, 0)$. If $f(w)$ is its complex velocity potential, then

$$f_1(w) = \frac{U_1}{U}f(w/k_1)k_1 \tag{3.34}$$

describes a flow past a body B_1 which can be obtained from B using a similarity transformation with coefficient k_1. The speed of the flow (3.34) at infinity is U_1. If $w_0 \in B$, then $w_1 = k_1 w_0$ is its corresponding point on B_1.

Since

$$\left.\frac{f_1'(w)}{U_1}\right|_{w=w_1} = \left.\frac{f'(w)}{U}\right|_{w=w_0},$$

the values of the scaled velocity u_e associated with the flows past B_1 and B taken at w_1 and w_0 respectively are the same. Furthermore, since the ratio of the characteristic lengths for B_1 and B is k_1, the value of the scaled arclength is the same for w_1 and w_0. This means that both flows yield the same $u_e(s)$ and so the equations (3.29)–(3.30) are invariant with respect to changes of the speed of the uniform flow and the scaling factor.

Computation of the inviscid speed uses the potential flow past an approximating ζ-profile. We cannot guarantee that this profile meets the condition (3.13) with sufficiently large γ. As a consequence, there will always be a singularity at the point where the approximate front face meets the upper/lower faces of the body. To overcome the resulting difficulty during the boundary layer computation we will be considering an extended front face

$$G_{\text{ext}}(x_w, y_w) = 0, \ \text{ where } G_{\text{ext}}(x_w, y_w) \equiv \begin{cases} G(x_w + T, y_w) = 0, & \text{if } x_w < -T \\ y_w^2 - H^2, & \text{if } x_w \geq -T \end{cases}$$

where $G(x_w, y_w) = 0$ is the equation of the original front face and $T > 0$. Such an extension is artificial, it does not change the geometry of the body and its aspect ratio. However, by shifting the singular points downstream it removes them from the segment of interest, on which boundary layer computation will be carried out.

Now introduce the family of "generalised ellipse" faces having

$$\frac{|x_w|^p}{L^p} + \frac{y_w^2}{H^2} = 1 \ . \tag{3.35}$$

This is elliptic if $p = 2$, but has a smoother behaviour near $x_w = 0$ if $p > 2$.

We will require that $p > 2$, which is needed for the continuity of the second derivative of the function describing the body profile.

For each fixed p, our aim is to find minimal L under which the boundary layer is not yet separated, or, equivalently, the skin friction factor τ is strictly positive.
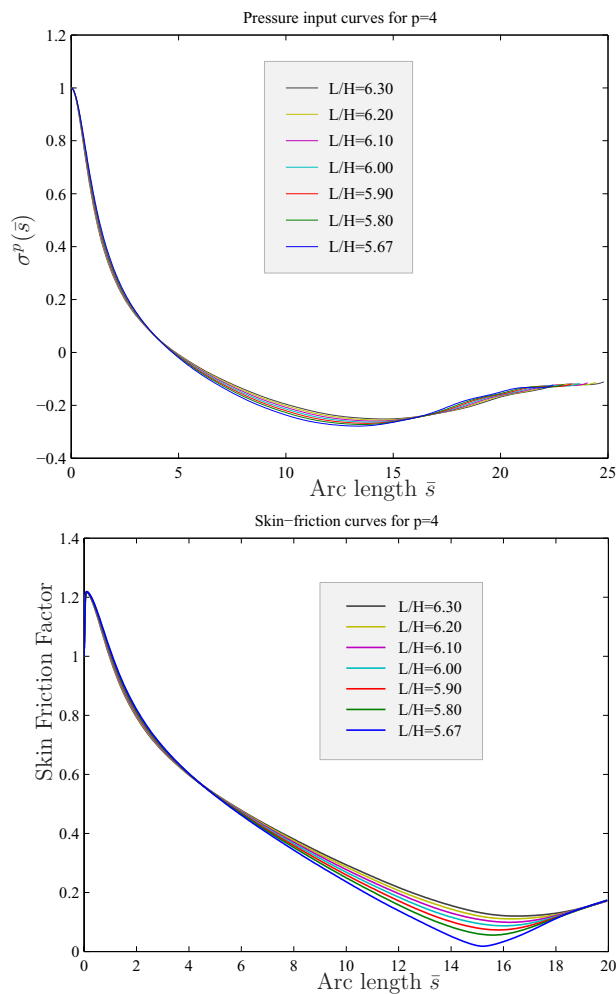

Figure 3.7: Determination of $L_{\min}(4)$

Assume that $H = \pi$. A computational cycle for each fixed p consists in generating skin friction factor distributions for a sequence of L. We start with a sufficiently large L and decrease it with a small step until reaching the value $L_{\min}(p)$ below which an unseparated flow can no longer exist. This is illustrated in Figure 3.7 for $p = 4$.

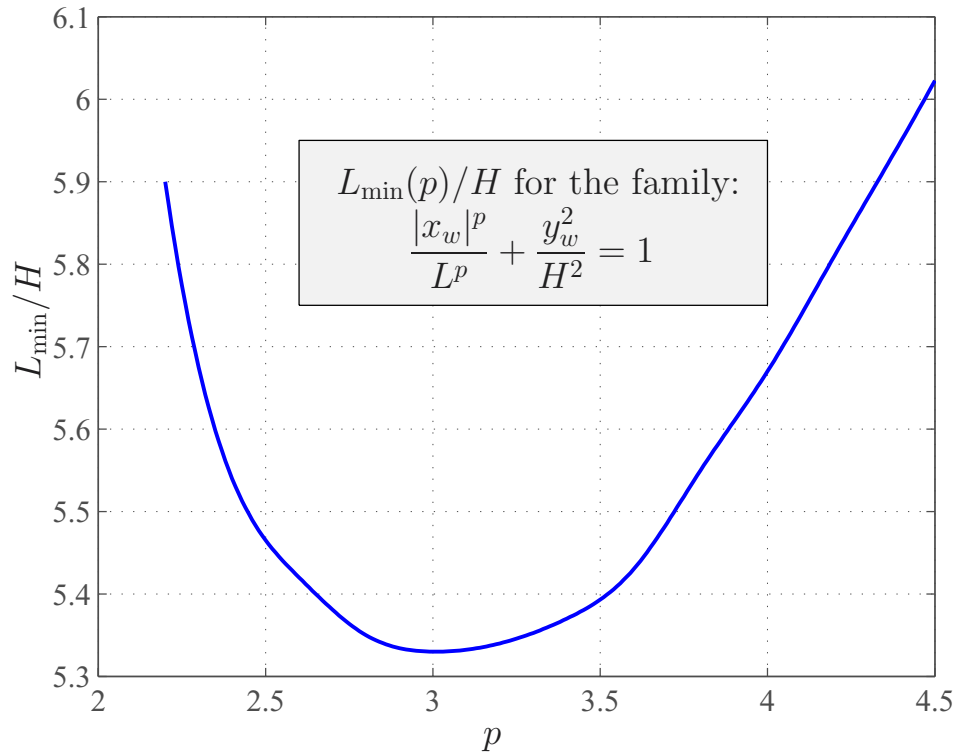The resulting plot of $L_{\min}(p)$ is shown in Figure 3.8.

The inset box reads:

$$L_{\min}(p)/H \text{ for the family:}$$
$$\frac{|x_w|^p}{L^p} + \frac{y_w^2}{H^2} = 1$$

Figure 3.8: Plot of $L_{\min}(p)/H$

Table 3.1 contains the data used for generating the plot in Figure 3.8.

p	2.2	2.3	2.4	2.5	2.6	2.7	2.8	2.9
$L_{\min}/H$	5.90	5.64	5.54	5.47	5.42	5.38	5.35	5.33

p	3.0	3.1	3.2	3.3	3.4	3.5	3.6	3.7
$L_{\min}/H$	5.33	5.33	5.34	5.35	5.37	5.39	5.43	5.49

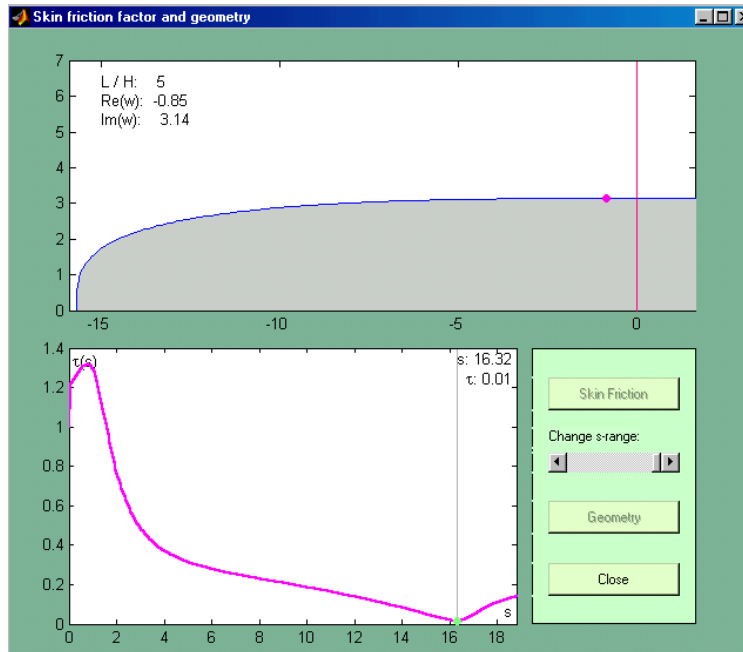| p	3.8	3.9	4.0	4.1	4.2	4.3	4.4	4.5
$L_{\min}/H$	5.55	5.62	5.67	5.75	5.81	5.88	5.95	6.03

Table 3.1: Results for the family (3.35)

Figure 3.9: Skin friction factor and geometry for (3.36) with $(p, q) = (3, 3.5)$

Figure 3.8 shows that the smallest ratio takes place at $p \approx 3$. Small further improvement, having the form of "diminishing returns", is possible if we

consider the family of front faces satisfying

$$\frac{|x_w|^p}{L^p} + \frac{|y_w|^q}{H^q} = 1 \,. \tag{3.36}$$

For example, if $p = 3$ and $q = 3.5$, then $L_{\min}/H$ is 5.0. The configuration corresponding to these values of parameters is shown in Figure 3.9.

We can see from Table 3.1 or from Figure 3.8 with $p = 4$, that for bodies with front faces satisfying

$$\frac{x_w^4}{L^4} + \frac{y_w^2}{H^2} = 1 \,, \tag{3.37}$$

a critical ratio L/H below which the flow can no longer be unseparated is approximately 5.67.
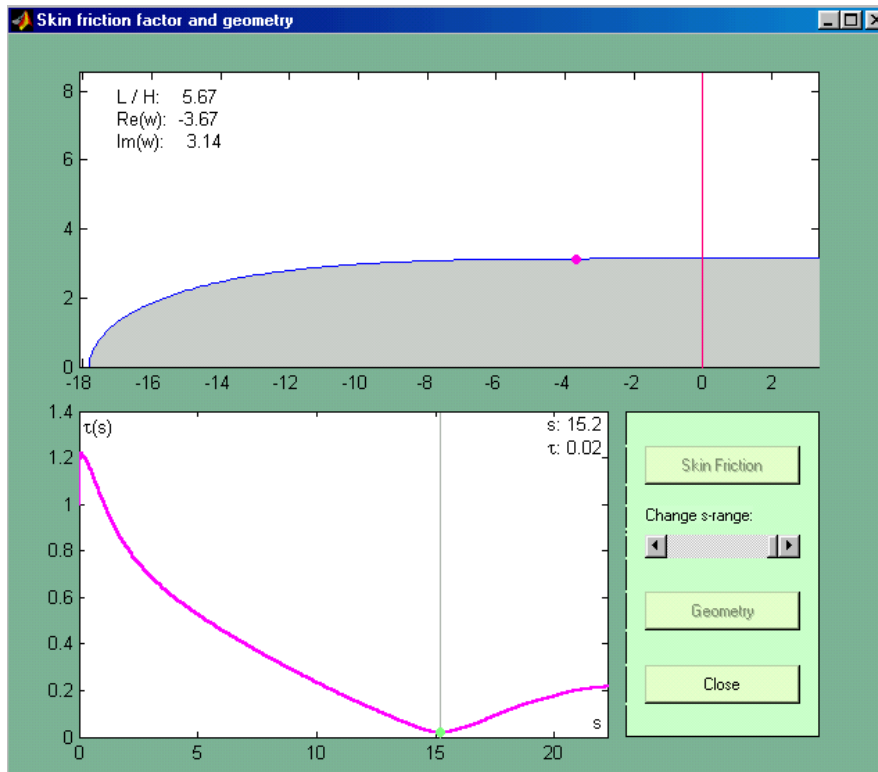

Figure 3.10: Skin friction factor and geometry for (3.37) with $L/H = 5.67$

Figure 3.10 shows the critical point in the physical plane where separation is likely to occur if the ratio L/H were made smaller noting that this point lies further ahead of the junction point $x = 0$ than for more-optimal configuration such as that in Figure 3.9.
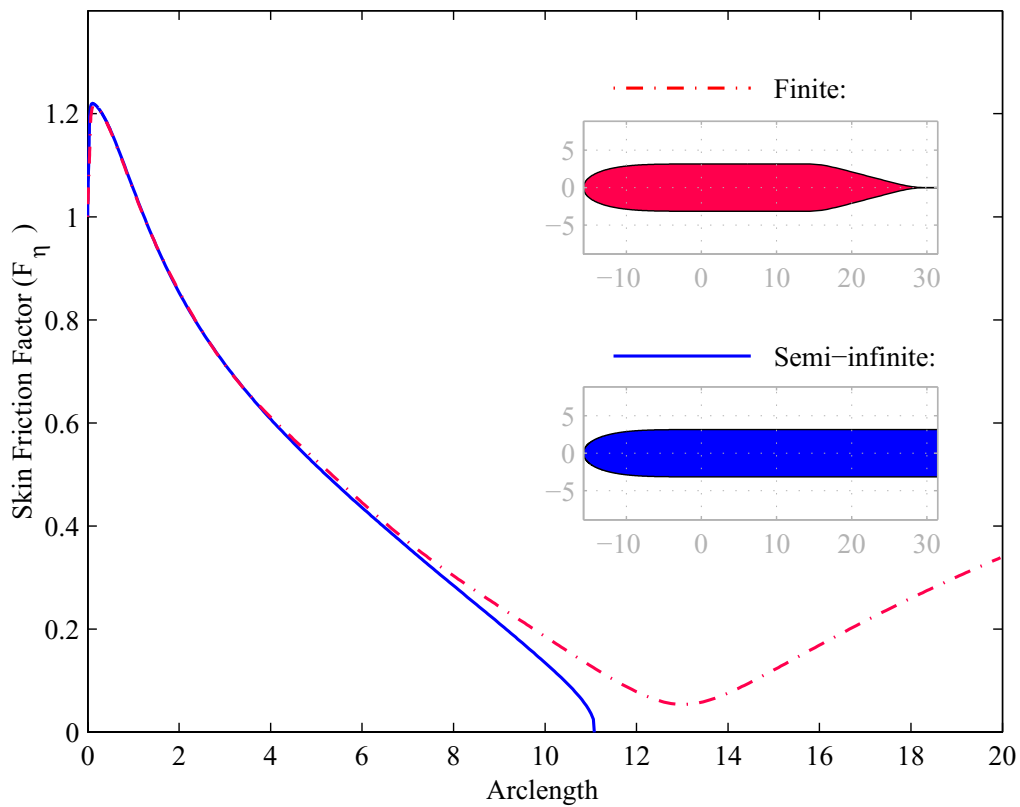

Figure 3.11: Plots of τ for finite and semi-infinite objects with $p = 4$.

The body in Figure 2.15 has $L/H = 5 < 5.67$, which suggests that for finite wings the critical aspect ratio is smaller. Figure 3.11 shows the plots of computed skin friction factor for a finite and semi-infinite bodies having the

same front face described by (3.37) with $L/H = 5$. We can see from this plot that the flow for a finite wing is unseparated, whereas the skin friction factor for the infinite object reaches zero, which is an indication of a separated flow.

For flow control purposes it might be interesting to know the location of the critical point corresponding to the minimal value of the skin friction factor. The plot in Figure 3.12 shows how the x-coordinate of such critical points for optimal representatives of family (3.35) with $H = \pi$ depends on p.
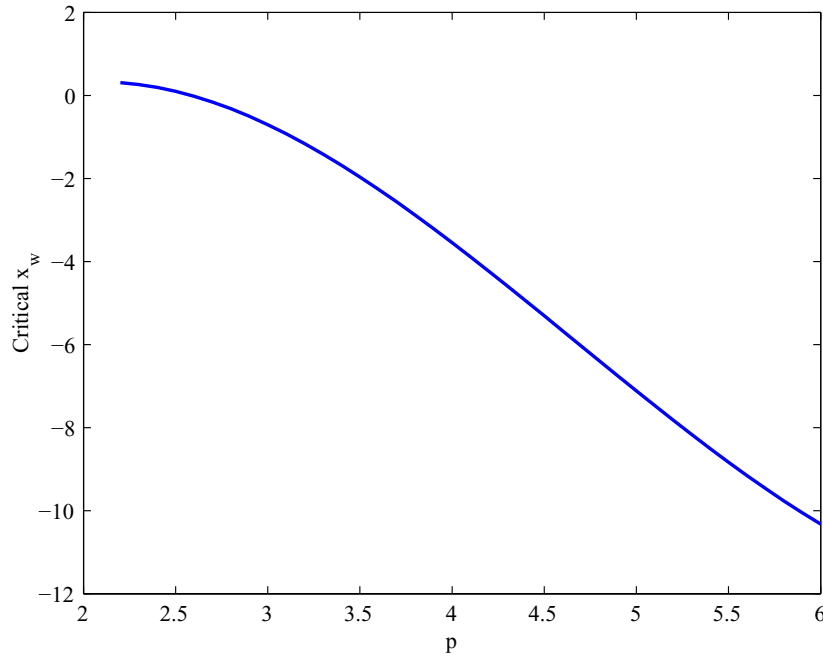

Figure 3.12: Location of the critical point as a function of p for (3.35)

We can see that, as the parameter p approaches 2, the critical value stabilizes near the point $x = 0$ where the front face joins the rest of the body.

We found that when $p = 2$ or when p was too close to this value, it was impossible to obtain unseparated flows by changing the L/H ratio, which we attribute to surface curvature discontinuity at the junction point $(x = 0)$ for purely elliptic noses.

The paper [5] considered the case of purely elliptic noses. In our opinion, such results can be only approximate, since the boundary layer will separate at the junction irrespective of the aspect ratio and we believe that a smoother matching $(p > 2)$ is needed to eliminate this type of separation.

Conclusion

In conclusion, we summarise the outcomes achieved in this work.

In Chapter 1 we considered a number of families of asymptotically parabolic nose shapes and suggested geometries which delay laminar boundary layer separation to larger angles of attack. Approximately, a 9% improvement compared to a purely parabolic nose case has been achieved for symmetric noses, and an 11% improvement for "drooped" noses.

In Chapter 2 we examined how the considerations used for the leading-edge region of thin airfoils apply to finite wings of arbitrary shape. We used the Theodorsen-Naiman method for inviscid flow computation. The corresponding methodology, implemented in the form of a graphical user interface in MATLAB, allows one to design a wing, set up computation parameters and control the convergence of the iterative procedure. For relatively short wings the laminar flow separation results have been shown to depend not only on the leading edge geometry but also on the geometry of the rest of the wing. We found that for longer wings the adopted method of computing inviscid flow fails because the role of higher harmonics in finite trigonometric series becomes dominating at the stage of solution of Prandtl's equations.

In Chapter 3 we addressed this problem by appropriately modifying the

procedure for inviscid flow computation, and making it suitable for long symmetric bodies. The resulting techniques have been applied to a particular family of front faces of length L and width H, to find the profile with minimal L/H ratio allowing an unseparated flow.

All applications and programs used in this work have been coded in C/C++ and MATLAB.

Bibliography

[1] I. H. Abbott and A. E. von Doenhoff. *Theory of wing sections*. Dover, New York, 1959.

[2] R. Agarwal. Computational fluid dynamics of whole body aircraft. *Ann. Rev. Fluid. Mech.*, 31:125–169, 1999.

[3] J. D. Anderson, S. Corda, and D. M. Van Wie. Numerical lifting line theory applied to drooped leading-edge wings below and above stall. *J. Aircraft*, 17:898–904, 1980.

[4] T. Cebeci, R. W. Clark, K. C. Chang, N. D. Halsey, and K. Lee. Airfoils with separation and the resulting wakes. *J. Fluid Mech.*, 163:323–347, 1986.

[5] M. R. Davis. Design of flat plate leading edges to avoid flow separation. *AIAA J.*, 18:598–600, 1979.

[6] A. S. Dostovalova. Airfoil nose shapes delaying leading-edge separation. *Fluid Mechanics Seminar*, Department of Applied Mathematics, 15 October 1999.

[7] M. Drela and M. B. Giles. Viscous-inviscid analysis of transonic and low Reynolds number airfoils. *AIAA J.*, 25:1347–1355, 1987.

[8] M. Drela and H. Youngren. *XFOIL 6.94 user guide*, Dec 2001.

[9] M. Gad-el-Hak, A. Pollard, and J.-P. Bonnet, editors. *Flow control: fundamentals and practices.* Lecture Notes in Physics 53. Springer, Berlin, 1998.

[10] N. D. Halsey. Potential flow analysis of multi-element airfoils using conformal mapping. *AIAA J.*, 17:1281–1288, 1979.

[11] M. R. Head. Approximate methods of calculating the two-dimesional laminar boundary layer with suction. In G. V. Lachman, editor, *Boundary layer and flow control: its principles and application*, volume 2, pages 801–841. Pergamon Press, Oxford, 1961.

[12] T. Itiro. History of boundary-layer theory. *Ann. Rev. Fluid. Mech.*, 9:87–111, 1977.

[13] R. D. Joslin. Aircraft laminar flow control. *Ann. Rev. Fluid. Mech.*, 30:1–29, 1998.

[14] H. B. Keller. Numerical methods in boundary-layer theory. *Ann. Rev. Fluid Mech.*, 10:417–433, 1978.

[15] L. D. Landau and E. M. Lifshitz. *Theoretical physics. Vol. VI. Hydrodynamics.* Nauka, Moscow, 1988.

[16] M. A. Lavrentjev and B. V. Shabat. *Hydrodynamical problems and their mathematical models.* Nauka, Moscow, 1977.

[17] R. H. Liebeck. Design of subsonic airfoils for high lift. *J. Aircraft*, 15:547–561, 1978.

[18] The MathWorks. *Using* MATLAB, 2000.

[19] J. A. Moriarty and E. O. Tuck. Thin airfoils with high-incidence flaps or blunt trailing edges. *Aeronaut. J.*, 93:93–99, 1989.

[20] N. I. Muskhelishvili. *Singular integral equations*. Groningen, P. Noordhoff, 1953.

[21] I. Naiman. Numerical evaluation of the ϵ-integral occurring in the Theodorsen arbitrary airfoil potential theory. Technical Report ARR L4D27a, NACA, 1944.

[22] I. Naiman. Numerical evaluation by harmonic analysis of the ϵ-function of the Theodorsen arbitrary potential theory. Technical Report ARR L5H18, NACA, 1945.

[23] J. N. Newman. *Marine Hydrodynamics*. MIT Press, Cambridge (Massachusetts), 1979.

[24] L. Rosenhead, editor. *Laminar boundary layers*. Clarendon Press, Oxford, 1963.

[25] A. I. Ruban. Asymptotic theory of short separation regions on the leading edge of a slender airfoil. *Izv. Akad. Nauk SSSR, Mekh. Zhidk. Gaza*, 1:42–51; English translation: *Fluid Dynamics* pp. 33–41, 1981.

[26] H. Schlichting. *Boundary-layer theory*. McGraw-Hill, New York, 1979.

[27] S. T. Simakov and A. S. Dostovalova. Interactive graphics in MATLAB. *PreJournal*, May 2001. Available at <http://www.prejournal.com>.

[28] S. T. Simakov, A. S. Dostovalova, and E. O. Tuck. A gui for computing flows past general airfoils. In *Australasian* MATLAB *Users Conference*. Ceanet, 2000. Available at <http://www.ceanet.com.au/mluserconf/papers.asp>.

[29] E. Stanewsky. Adaptive wing and flow control technology. *Progress in Aerospace Sciences*, 37:583–667, 2001.

[30] Vladimir V. Sychev, A. I. Ruban, Victor V. Sychev, and G. L. Korolev. *Asymptotic theory of separated flows*. Cambridge University Press, 1998.

[31] T. Theodorsen. Theory of wing sections of arbitrary shape. Technical Report Rept. 411, NACA, 1931.

[32] T. Theodorsen and I. E. Garrick. General potential theory of arbitrary wing sections. Technical Report Rept. 452, NACA, 1933.

[33] E. O. Tuck. A criterion for leading edge separation. *J. Fluid Mech.*, 222:33–37, 1991.

[34] E. O. Tuck and A. S. Dostovalova. Airfoil nose shapes delaying leading-edge separation. *Aeronaut. J.*, 104:433–437, 2000.

[35] M. D. Van Dyke. Subsonic edges in thin-wing and slender-body theory. Technical Report TM 3843, NACA, 1954.

[36] M. J. Werle and R. T. Davis. Incompressible laminar boundary layers on a parabola at angle of attack: A study of the separation point. *Trans. ASME: J. Appl. Mech.*, pages 7–12, March 1972.

[37] W. Wuest. Survey of calculation methods of laminar boundary layers with suction in incompressible flow. In G. V. Lachman, editor, *Boundary layer and flow control: its principles and application*, volume 2, pages 771–800. Pergamon Press, Oxford, 1961.